

# Progress in the Development of Broadly Reactive Norovirus Therapeutics

Grant S. Hansman

[g.hansman@griffith.edu.au](mailto:g.hansman@griffith.edu.au)

Gargi Kher

Anna D. Svirina

Jeremy R.H.Tame

Lauren Hartley-Tassell

Hiro Irie

Mark von Itzstein

Penny A. Rudd

Marie Pancera

[mpancera@fredhutch.org](mailto:mpancera@fredhutch.org)

---

## Research Article

### Keywords:

**Posted Date:** February 26th, 2024

**DOI:** <https://doi.org/10.21203/rs.3.rs-3980499/v1>

**License:**   This work is licensed under a Creative Commons Attribution 4.0 International License.

[Read Full License](#)

**Additional Declarations:** The authors declare no competing interests.

---

## **Progress in the Development of Broadly Reactive Norovirus Therapeutics**

Grant S. Hansman<sup>1,#</sup>, Gargi Kher<sup>2</sup>, Anna D. Svirina<sup>3</sup>, Jeremy R.H. Tame<sup>4</sup>, Lauren Hartley-Tassell<sup>1</sup>, Hiro Irie<sup>1</sup>, Mark von Itzstein<sup>1</sup>, Penny A. Rudd<sup>1</sup>, and Marie Pancera<sup>2,#</sup>

<sup>1</sup>Institute for Glycomics, Griffith University, Gold Coast Campus, Gold Coast, QLD, Australia

<sup>2</sup>Vaccine and Infectious Disease Division, Fred Hutchinson Cancer Center, Seattle, WA, USA

<sup>3</sup>Octapharma Biopharmaceuticals GmbH, Heidelberg, Germany

<sup>4</sup>Graduate School of Medical Life Science, Yokohama City University, Tsurumi, Yokohama, Japan

<sup>#</sup>Corresponding authors

**Abstract**

Discovered over five decades ago, norovirus is frequently reported as the leading cause of outbreaks of acute gastroenteritis. No vaccines or antivirals are currently available. We further analyzed two of our leading norovirus inhibitors that either indirectly or directly obstructed norovirus from binding to histo-blood group antigen receptors. Using X-ray crystallography, we showed that both inhibitors engage highly conserved capsid residues amongst genetically diverse noroviruses. The indirect inhibitor, a modified Fc-linked Nanobody, showed improved binding affinity and neutralization capacity compared with the native Nanobody. More strikingly, we showed that the direct inhibitor, a chewable prebiotic tablet containing human milk oligosaccharide 2'-fucosyllactose, worked as an inhibitor for a leading norovirus. These new discoveries are expected to promote the development of effective norovirus treatments.

**One-Sentence Summary**

We engineered and improved a norovirus antibody-based antivirals and showed a chewable trisaccharide tablet inhibited the principal norovirus.

## Main Text

### Introduction

Noroviruses are highly contagious and since there are currently no treatments available, outbreaks continue to shut down hospital wards, day-care centers, schools, aged care facilities, and cruise ships (1). Infections typically cause nausea, vomiting, severe abdominal pain, diarrhea, and fever. Human norovirus has a positive sense RNA genome of ~7.7 kilobases with three open reading frames (ORF1-3), encoding non-structural proteins, a capsid protein (VP1), and a small protein, respectively. At least ten genogroups exist (termed GI-GX) that are divided into a plethora of genotypes, genetic variants, and recombinants (2). Norovirus GII has at least 29 genotypes (2), most of which are antigenically distinct (3), although genotype 4 (GII.4), GII.17, and related genetic variants have caused most large outbreaks over the two past decades (2).

Expression of the capsid gene in insect cells typically leads to the self-assembly of virus-like particles (VLPs) that are morphologically and antigenically similar to native norovirus virions, i.e., 180 copies of VP1 with T=3 icosahedral symmetry (4). The capsid protein is divided into two main domains termed shell (S) and protruding (P), which are linked by a flexible hinge of 10-15 residues. Based on the X-ray structure, the P domain is further subdivided into P1-1, P2, and P1-2 subdomains. The P2 subdomain is the most exposed and varied at the amino acid level compared to other (sub)domains (4-6). Noroviruses require histo-blood group antigen (HBGA) receptors for an infection to occur (7, 8). Using X-ray crystallography, at least eight different HBGA types (e.g., A-, B-, H2-, Lewis Y-type) were shown to bind to the top of the P2 subdomains (5, 6, 9-17). HBGA can be complex carbohydrates linked to proteins, lipids present on epithelial, and other cells in the body or found as free antigens (for example in saliva). Blocking norovirus attachment to HBGA is one of the main objectives in vaccine and antiviral development followed by broad reactivity.

Presently, several companies are evaluating norovirus VLP vaccine candidates in human clinical trials with research costs already exceeding \$200 million (18-22). The purpose of the non-replicating VLP immunogens is to elicit cross-reactive (genogroup/genotype), neutralizing, long-term antibodies. The most advanced vaccine candidate is in Phase 2b (NCT05281094; testing efficacy and safety in healthy children) with a bivalent formulation of GI.1/GII.4c VLPs (21-24), where the GII.4c was engineered with a “consensus sequence” of three GII.4 variant sequences to broaden the immune response (25, 26).

Recently, we and others developed norovirus specific Nanobodies using norovirus VLPs (27-35). Nanobodies are small (~15 kDa), single domain antibodies, with three complementarity determining regions (CDRs), strong-antigen binding affinities, and low immunogenicity (36). Our group identified two high-affinity Nanobodies (termed NB26 and NB85) that cross-reacted against several GII genotypes (GII.1, GII.2, GII.4, GII.10, and GII.17) (33, 34). Using X-ray crystallography, we showed NB26 and NB85 bound to occluded regions on the P domain and indirectly inhibited VLPs binding to HBGA in a surrogate neutralization assay. In another study, we showed a combination of NB85 and laboratory grade human milk oligosaccharide (HMO) 2'-fucosyllactose (2'-FL) had an additive effect on GII.10 VLP inhibition, while another GI-specific Nanobody in combination with 2'-FL had a synergic effect on GI.1 VLP inhibition (32). We also showed that 2'-FL bound directly at the GI.1, GII.10, and GII.17 HBGA binding pockets using X-ray crystallography (13, 37).

In this study, we describe structural and functional properties of a modified NB26 and consumer grade 2'-FL products. To accurately define GII antigenic variation, we determined



the X-ray crystallography structures of GII.8, GII.14, GII.17, GII.24, GII.26, and GII.NA1 P domains. We also dimerized native NB26 using an IgFc (termed Fc-NB26) and examined both native NB26 and Fc-NB26 neutralization capacities using a human intestinal enteroid (HIE) culture system. Interestingly, we also showed that FDA and EU approved 2'-FL products sold online function as natural, cheap inhibitors that target the predominant GII.4 noroviruses.

## Results

**A conserved dynamic HBGA pocket is observed for many GII genotypes.** The X-ray crystal structures of GII.8, GII.14, GII.17-variant, GII.24, GII.26, and a non-assigned genotype (GII.NA1) P domains were solved to 1.27-1.74 Å resolution. (**Table S1**). Norovirus P domains expressed in *E. coli* typically form a biologically relevant homodimer ([6](#)) and like other structures, these six P1 subdomains are comprised of eight  $\beta$ -strands and one  $\alpha$ -helix, while the P2 subdomains contain six  $\beta$ -strands (**Fig. 1A**). These six P domains were structurally equivalent with a root mean square deviation (RMSD) for C-alpha atoms of 0.67-0.94 Å. The principal structural variation among the models is a variable length P2 subdomain loop, which we termed Loop A (chain A residues ~337-354). Loop A is 5-7 residues longer in GII.24, GII.26 and GII.NA1 P domains compared to GII.8, GII.14, and GII.17 P domains (**Figs. 1A, S1, and Table S2**). An extended Loop A is also present in GII.2, GII.6, and GII.10, and GII.19 P domains, whereas a shortened Loop A is found in GII.1, GII.3, GII.4, GII.11, and GII.12 P domains (**Figs. 1C, S1, and Table S2**). The X-ray crystal structures of these six P domains in complex with HBGAs is not yet determined, but superposition with a GII.10 P domain A-type trisaccharide complex structure revealed a conserved set of residues capable of interacting with the fucose moiety of HBGAs. These include side- (underlined) and main-chain interactions for GII.8 (residues T346, R347, D375, and G440), GII.14 (residues T345, R346, D374, and G439), GII.17 (residues T349, R350, D378, and G443), GII.24 (residues N354, R355, D384, and G446), GII.26 (residues N353, R354, D383, and G445), and GII.NA1 (residues N354, R355, D384, and G446) (**Figs. 1B**).

Structural analysis of other GII X-ray crystal structures shows that, in at least 15 genotypes and closely matching genetic variants, conserved fucose binding residues are present ([6](#), [9](#), [13](#)). Our analysis shows the HBGA binding pocket is formed by a quaternary interaction at the P domain dimeric interface involving loops from chains A and B. Loop A (chain A residues ~337-354), described above, together with Loop B (chain A residues ~371-391), Loop D (chain A residues ~390-407), and Loop C (chain B residues ~434-454) form the main HBGA pocket (**Figs. 1 and S1, Table S2**). At its base, Loop A contains a conserved arginine residue whose side chain binds the fucose moiety of HBGAs. Loop B has a highly conserved, well-positioned aspartic acid, which forms two direct hydrogen bonds with the fucose moiety of HBGAs. Loop C has one main chain residue that almost always forms a direct hydrogen bond with the fucose moiety (**Figs. 1B and 1C**) ([6](#), [9](#)). The placement of Loops B and C are also conserved in these novel structures, whereas Loop D is more variable in length among the genotypes. Also, Loop D contains a few variable residues that loosely bind (e.g., through water mediated interaction) HBGA saccharides other than fucose ([6](#), [9](#), [14](#)). Overall, the dynamics of the HBGA binding pocket is mainly formed by quaternary interactions, with three main loops, Loops A and B (chain A) and Loop C (chain B) strongly holding the fucose. The amino acid variation surrounding the HBGA pocket might select for different HBGA types among the human population ([9](#), [13](#), [38](#)), thus increasing norovirus infection rates by binding to multiple HBGA types while at the same time escaping from host immune responses. Of note, two P domains in this analysis (GII.11 and GII.19) were isolated from pigs (**Table S2**), stressing that these important structural features are shared with animal noroviruses.

The engineered GII.4c VLP introduces variability near the HBGA pocket. To precisely compare the engineered GII.4c immunogen with natural genetic diversity, the first X-ray crystallographic structure of the GII.4c P domain was solved at 1.34 Å resolution (**Fig. 2A and Table S3**). Like all other native GII.4 P domains, the GII.4c P domain is subdivided into the P1 subdomain (residues 225-281 and 421-530) with eight  $\beta$ -strands and one  $\alpha$ -helix and P2 subdomain (residues 282-420) with six  $\beta$ -strands. Nine of thirteen amino acid substitutions in GII.4c are exposed on the surface of the P2 subdomain and several residues (S372, F375, and S393) sit in the HBGA pocket (**Fig. 2B**). To better understand if these amino acid substitutions affected HBGA binding interactions at the atomic level, we determined the X-ray crystallographic structure of the GII.4c P domain in complex with H2-type at 1.61 Å resolution (**Fig. 2A and Table S3**). The H2-type consists of an  $\alpha$ -L-fucose-(1-2)- $\beta$ -D-galactose-(3-1)-2-N-acetyl- $\alpha$ -D-galactosamine, however, only the fucose and galactose moieties were sufficiently ordered to be modeled into the electron density map (**Fig. S3**). Unfortunately, the GII.4c P domain did not form complexes with any other HBGA types, regardless of soaking and co-crystallization conditions. Nevertheless, the GII.4c P domain interacts with the fucose moiety of H2-type through a set of highly conserved residues (R345, T344, D374, and Y444), which were not substituted in the engineered immunogen (**Fig. 2B**). Comparing the GII.4c substitutions with an amino acid diversity plot of GII.4 genetic variants showed that many substitutions are in variable patches on the P2 subdomain surface (**Figs. 2C and 2D**). When the amino acid diversity is mapped using one representative from each of the 29 genotypes, most of the top surface of the P2 subdomain is highly variable, except for the two HBGA pockets and the lateral region between the HBGA pockets (**Fig. 2E**). We previously showed that this conserved region binds two additional fucose subunits on the GII.10 P domain (**Fig. 2E**), although the function(s) of the fucose binding sites remains unclear ([39](#)). Overall, our extensive structural analysis of 15 genotypes supports the notion that this HBGA pocket is relatively conserved, making it an attractive universal norovirus infection therapeutic target. However, the HBGA pocket is also surrounded by loops differing in length and containing extensive amino acid diversity (**Fig. S4**), both of which, represent important capsid functions/features that most likely contribute to viral escape through temporal capsid evolution. As such, we and others have yet to discover high affinity, broadly neutralizing antibodies or Nanobodies that bind to this HBGA pocket ([40, 41](#)).

**An engineered Fc-linked Nanobody (Fc-NB26).** To convert the broadly reactive NB26 into a next generation therapeutic, we linked the C-terminus of the Nanobody onto a human Fc sequence and expressed the modified Nanobody (termed Fc-NB26) in insect cells (**Fig. S5**). Similar modifications have improved inhibition capacities for viruses such as HIV and COVID-19 ([42-46](#)). A direct ELISA was used to evaluate the cross-reactive binding capacity of Fc-NB26 with numerous GII genotypes (GII.4, GII.8, GII.10, GII.14, GII.17, GII.24, GII.28, and GII.NA1) (**Fig. 3A**). Fc-NB26 bound to these eight genotypes, including the GII.4 variants, at concentrations ranging from 5-78 ng/mL, equivalent to NB26 which detected GII.1, GII.2, GII.4, GII.10, and GII.17 VLPs ([30, 33](#)). Superposition of the structure of a GII.10 P domain bound to NB26 with GII.8, GII.14, GII.17, GII.24, GII.28, GII.NA1 P domain structures revealed no steric clashes with NB26 (**Figs. 3B and 3C**). Interestingly, we note that a recently described neutralizing Nanobody (termed M4) bound at a site overlapping the NB26 epitope and shared several equivalent hydrogen bond interactions in this cavity (**Fig. 3D**) ([33-35](#)), despite extensive genetic diversity between the CDR sequences (**Fig. S6**). The binding affinities of Fc-NB26 and NB26 to GII.4-Syd and GII.10 P domains were measured using ITC (**Fig. S7**). The affinities of NB26 to GII.4-Syd and GII.10 were similar, with  $K_d$  values of 441 nM and 427 nM, respectively. As expected for a dimeric molecule, the affinities of Fc-NB26 to GII.4-Syd and GII.10 P domains were significantly higher than NB26, with  $K_d$  values of

5.87 nM and 0.82 nM, respectively, and a stoichiometric ratio of ~2:1 (Students' T-test, P value < 0.05).

Our previous studies showed that NB26 blocked GII.4 and GII.10 VLPs from binding to HBGAs in a surrogate HBGA blocking assay (33). To further examine the therapeutic potential of NB26 and Fc-NB26, we analyzed the neutralization using the norovirus HIE culture system with a GII.4 norovirus (Fig. 3E). We found that NB26 neutralized norovirus replication with an IC<sub>50</sub> value of 104.6 ng/mL (~7.0 nM), whereas Fc-NB26 neutralized with an IC<sub>50</sub> value of 15.5 ng/mL (~1.0 nM) (Fig. 3F). The NB26 and Fc-NB26 neutralization results were comparable to the M4 Nanobody with IC<sub>50</sub> values ranging between 53-379 ng/mL (4-25 nM) for different GII.4 variants (35). Similarly, a GII.4 specific IgG Mab (termed 10E9) neutralized a GII.4 variant with an IC<sub>50</sub> value of 97 ng/mL (~0.6 nM) (41). Likewise for GV murine norovirus, we previously identified several Nanobodies (NB5820 and NB5829) that neutralized murine norovirus in cell culture with IC<sub>50</sub> values between 40-900 ng/mL (2-60 nM) (31). Finally, to better comprehend the neutralization mechanism of Fc-NB26, we examined untreated, NB26 treated, and Fc-NB26 treated GII.10 VLPs using negative stain electron microscopy. Untreated GII.10 VLPs had a similar morphology to NB26 treated GII.10 VLPs, whereas Fc-NB26 treated GII.10 VLPs clearly resulted in particle disassembly and aggregation (Fig. 3G).

**Readily available 2'-FL inhibits norovirus.** Recently, different consumable forms of 2'-FL have been made available online. We tested the inhibition potential of a 98% pure 2'-FL powder and chewable 2'-FL tablets with GII.4-Syd, since its P domain binds numerous HBGA types (9). We showed that GII.4-Syd VLP bound to human A-type saliva (a source of HBGAs) in a dose-dependent manner (Fig. 4A). Additionally, both the 2'-FL powder and chewable 2'-FL tablets inhibited VLP binding to A-type saliva with IC<sub>50</sub> values of 7.5 mM and 36 mM, respectively (Fig. 4B). This result was comparable to our previous 2'-FL inhibition studies with GI.1, GII.10, and GII.17 VLPs with IC<sub>50</sub> values ranging between 11-38 mM (13, 37). To complement our ELISA data and confirm that 2'-FL bound at the HBGA pocket, we determined the X-ray crystal structures of GII.4 and GII.10 P domains in complex with 0.25 mg/mL solutions of the 2'-FL powder or chewable tablet at 1.41-1.54 Å resolution. (Fig. 4C and Table S4). The 2'-FL is a trisaccharide composed of an α-L-fucose-(1-2)-β-D-galactose-(1-4)-α-D-glucose. The electron density was well-defined for all three saccharides in all three structures (Fig. S3). The 2'-FL formed a network of hydrophilic and hydrophobic interactions at the dimeric interface which were comparable to previous 2'-FL complex structures we solved for GII.10 and GII.17 P domains (Figs. 4D, 4E, and 4F) (13, 37). Our results show that P domain residues that regularly interact with the fucose moiety of HBGAs also bind the fucose moiety of 2'-FL, whereas the galactose and glucose moieties of 2'-FL were held less strongly, comparable to previous complex structures our group determined (6, 9, 13, 37, 47). Overall, structural association of 2'-FL and different HBGA types in complex with GII.4 and GII.10 P domains showed that the fucose moieties were anchored at the same position (Fig. 4G). For GII.4, the bound 2'-FL mimicked the first three saccharides of H2, Lewis-Y, Lewis-X, and Lewis-B, whereas the second and third saccharides of A-type and B-type HBGAs kink up and turn away from this orientation (Fig. 4H). A similar arrangement was observed for GII.10, except that in the bound H2 complex the second and third saccharides deviated from this orientation (6, 47).

## Conclusions

Our data showed that the norovirus GII HBGA binding pocket uses a regular set of 3 to 5 fucose binding residues. The extensive amino acid variation just beyond and surrounding this

small set fucose binding residues is likely an evolutionary mechanism to avoid immune surveillance and a shared strategy among the GII genotypes. We previously screened Nanobody libraries developed against GII.4, GII.10, and GII.17 VLPs and discovered four Nanobodies that directly bound at the HBGA pockets but were genotype specific (33, 34, 40). Similarly, mAbs with neutralization capacities that bind on the top of the P2 subdomain and even the side of the P domain are mainly genotype specific (41, 48, 49). Thus, we focused our attention on further developing NB26 that bound at a highly conserved occluded region on the capsid and showed had therapeutic potential. Here, we found that NB26 modifications into an Fc-linked Nanobody improved binding affinities and increased neutralization capacities, as has been found to improve biochemical functions and inhibition for viruses such as HIV and COVID-19 (42-46). Our structural data suggests that Fc-NB26 could bind most GII genotypes. Development of such broadly reactive potent therapeutic norovirus Nanobodies delivered as a slow releasing prophylactic would be of exceptional value for norovirus outbreaks, especially for the prevention or treatment of severe acute gastroenteritis in high-risk groups such as the young, elderly, and immunocompromised. Another finding from this study was proof that 2'-FL inhibits GII.4 binding to HBGAs. This is an important outcome, since the GII.4 is a principal cause of large outbreaks of acute gastroenteritis worldwide and a leading genotype in most sporadic infections. Furthermore, structural analysis indicated that most other GII genotypes containing the conserved HBGA binding residues could also be targeted with 2'-FL therapeutics. Interestingly, the FDA and EU considers 2'-FL to be safe, and it was reported that infants and young children could consume 2'-FL at concentrations up to 1.2 g/L per day (50). Thus, it is conceivable that 2'-FL would bind to norovirus virions, possibly reducing the numbers of infectious virus particles that can attach to HBGA receptors present on epithelial cells. It remains to be tested whether this affordable, readily available 2'-FL tablet works effectively as antiviral or prophylactic in a clinical setting, but a future clinical trial with 2'-FL appears warranted.

## Acknowledgments

We greatly appreciate the support staff and use of MX1 and MX2 beamlines at the Australian Synchrotron, Australia. We thank Anna Prewitt, Todd Reese, and Isabelle Kim for their help with refining the X-ray structures and Asma Talukder with protein purification.

## Funding

Funding for this study was provided by CHS foundation (Germany), Deutsche Forschungsgemeinschaft (DFG, FOR2327, Germany), and Griffith University (GSH).

## Author contributions

GSH: Protein design/expressi on/purification/crystallization, X-ray data collection/structural refinement, analysis of inhibition, cross-reactivity, figure design and production, manuscript drafting/preparation/writing/editing

GK: Structural refinement, manuscript writing/editing

ADS: Protein expression, organoid cell culture, analysis of inhibition, manuscript editing

JRHT: Structural refinement, manuscript editing

HI: Protein expression, crystal screening, manuscript editing

LHT: Affinity measurements, manuscript editing

MvI: Manuscript editing

PAR: Analysis of inhibition, crystal screening, manuscript editing

MP: Structural refinement, manuscript writing/editing



## Competing interests

Authors declare that they have no competing interests.

## Data and materials availability

All data are available in the main text or supplementary. Coordinates and structure factors for all X-ray crystallography structures solved in this study have been deposited to the Protein Data Bank under accession codes (PDB ID): GII.8 Amsterdam (8V95), GII.14 M7 (8V96), GII.17 CS-E1 (8V97), GII.24 Loreto 1972 (8V98), GII.26 Leon 4509 (8V99), GII.NA1 Loreto 1257 (8V9A), apo-GII.4c (8VRU), GII.4c H2-type (8VRV), GII.4-Syd 2'-FL powder (8Y5V), GII.10 2'-FL powder (8Y6C), and GII.10 2'-FL tablet (8Y6D).

## Figures

**Figure 1. Structures of novel GII P domains reveals a conserved HBGA pocket.** (A) The X-ray crystallography structures of GII.8, GII.14, GII.17, GII.24, GII.26, and GII.NA1 P domains shown in cartoon representation are mainly equivalent with each other and form a homodimer (i.e., chains A and B). The six P domains were colored as previously (6, 9), i.e., chain A P1/ chain A P2 / chain B P1 / chain B P2: GII.8 (brown/ deeptea/ yelloworange/ dirtyviolet), GII.14 (hotpink/ cyan/ green/ orange), GII.17 (teal/ forest/ sand/ bluewhite), GII.24 (aquamarine/ blue/ red/ orange/), GII.26 (yelloworange/ purple/ smudge/ brown), and GII.NA1 (pink/ greencyan/ palecyan/ lightmagenta). (B) Superposition of these six P domains, highlighting Loop A for GII.8 (dirtyviolet), GII.14 (cyan), GII.17 (forest), GII.24 (blue), GII.26 (brown), and GII.NA1 (lightmagenta). A GII.10 P domain A-type complex structure (PDB ID: 3PA1) was superimposed showing the A-type as green sticks. Closeup (right-side) on the conserved residues binding the fucose moiety of HBGA shown as side-chains or main chains (GII.8 residue numbering). The fucose, galactose, and galactosamine of the HBGA A-type are labeled as Fuc, Gal, and A2G, respectively. (C) Superposition of 15 genotype P domain structures with Loops A, B, C, and D highlighted. The loops were colored as above and with GII.1 (yellow), GII.2 (hotpink), GII.3 (lightblue), GII.4 (lime), GII.6 (lightorange), GII.10 (chocolate), GII.11 (forest), GII.12 (salmon), and GII.19 (deepblue). The GII.13 (PDB ID: 6JYR) and GII.21 (PDB ID: 4RM0) P domains have unique HBGA binding sites and were omitted from the analysis. The GII.10 P domain A-type complex structure (PDB ID: 3PA1) was superimposed showing the A-type as green sticks and the HBGA pocket (black circle) surrounded by variable length Loops A and D. Structures are shown from the top and side views. Closeup (right side) highlighting known GII.10 P domain binding residues N355, R356, D385, and G451 within these loops (labeled and shown as sticks) (6, 9).

**Figure 2. Structure of the engineered GII.4c P domain.** (A) The X-ray crystallography structures of the apo GII.4c P domain and H2-type trisaccharide complex are shown in cartoon representation. Only one H2-type molecule bound to the GII.4c P domain dimer and is shown in pale yellow sticks. (B) The GII.4c P domain H2-type complex structure is superimposed with a GII.4 Saga P domain H2-type complex structure (PDB ID: 4WZK, shown in green sticks) for comparison. The GII.4c amino acid substitutions are shown as side chains on the GII.4c P domain in pink sticks (25) and GII.4 Saga P domain in orange sticks. The closeup (right-side) shows the regular fucose binding residues (labeled and underlined), and amino acid substitutions for GII.4c (pink sticks) (25) and GII.4 Saga (orange sticks). The fucose (Fuc) interacts with GII.4c P domain residues G443, D374, R345, T344, and Y444, whereas S442 interacts with galactose (Gal). (C) Surface representation of GII.4c P domain (top and side views) showing the substituted amino acids and HBGA H2-type superimposed from the GII.4c complex structure. The GII.4c amino acid substitutions are colored cyan and a region of

substitutions are circled. Only one set of substitutions are labeled or circled on the dimer for clarity. **(D)** Surface representation of the GII.4-Syd P domain dimer showing amino acid diversity plot of 2000 different GII.4 sequences. The GII.4 Saga H2-type complex structure (PDB ID: 4WZK) was superimposed to show the HBGA binding site (H2-type, green sticks). The surface color-coded conservation ranged from highly conserved amino acids (purple) to highly variable (white). Predicted highly variable hotspots on the surface of the P domain are labeled and circled and are in comparable regions on the GII.4c P domain. **(E)** Surface representation of the GII.10 P domain dimer showing amino acid diversity plot of 29 GII genotype sequences. The GII.4 Saga H2-type complex structure (PDB ID: 4WZK) and GII.10 P domain fucose complex structure (PDB ID: 4Z4R) were superimposed to show the HBGA (H2-type, green sticks) and fucose binding sites (fucose, blue sticks).

**Figure 3. Fc-NB26 characterization.** **(A)** Cross-reactivity of Fc-NB26 to GII.4-CHDC, GII.4c, GII.4-Syd, GII.8, GII.10, GII.14, GII.17-Cs-E1, GII.24, GII.26, and GII.NA1 P domains using a direct ELISA. Error bars are shown. **(B)** Superposition of GII.10 P domain NB26 complex (PDB ID: 5O04) and the six novel P domain structures (gray cartoons) reveals a conserved NB26 binding pocket. **(C)** Closeup of NB26 binding site showing GII.10 P domain residues (labeled and colored yelloworange) and matching GII.8, GII.14, GII.17-Cs-E1, GII.24, GII.26, and GII.NA1 P domain residues that could interact with NB26. Figure S1 highlights NB26 binding site on an amino acid sequence alignment. **(D)** Surface representation of the GII.10 P domain (light and dark grey monomers) with overlapping M4 (PDB ID: 8G0W, magenta) and NB26 epitopes (GII.10 residues D269, L272, G274, and T276, shaded cyan). NB26 CDR1 R26 (side chain sticks, cyan) and M4 CDR3 R100 (side chain sticks, magenta) bind in this small cavity, with both arginine side chains forming several direct hydrogen bonds with the P domain residues. **(E)** Inhibition of human norovirus by NB26 and Fc-NB26 using a HIE culture system with a GII.4 stool sample. PBS was used as negative control. Error bars are shown. **(F)** Norovirus replication curves for NB26 and Fc-NB26. Error bars are shown. **(G)** Negative stain electron microscopy micrographs of GII.10 VLPs untreated, treated with NB26, and treated with Fc-NB26. One representative micrograph is shown for each condition. The black arrow shows particle aggregation, and the white arrows show particle disassembly and aggregation. Scale bar represents 200 nm.

**Figure 4. HMO 2'-FL is a broadly reactive weak inhibitor.** **(A)** Human A-type saliva was used to capture GII.4 VLPs in a direct ELISA. **(B)** The ELISA data showing 2'-FL powder (cyan sticks) and chewable tablet (blue sticks) inhibition of GII.4 VLPs binding to A-type saliva. The 2'-FL concentration on the X-axis represented the amount used from the powder and chewable tablet. **(C)** The X-ray crystal structures of GII.4 and GII.10 P domains bound to 2'-FL are shown as cartoons (note: the X-ray structure of GII.4 P domain 2'-FL complex is shown as a dimer). Three 2'-FL molecules from the powder bound per GII.10 P domain dimer, two at the typical HBGA binding sites and one at a non-specific contact indicated with an “\*”. One 2'-FL molecule from the 2'-FL chewable tablet bound per GII.10 P domain dimer. **(D)** Close-up of 2'-FL (powder, cyan sticks) binding interaction with the GII.4 P domain, showing 2'-FL: fucose (Fuc), galactose (Gal), and glucose (Glc). **(E)** Close-up of GII.10 P domain 2'-FL complex structure (powder) showing the binding interactions with 2'-FL shown in sticks and labeled (an comparable interaction for 2'-FL was observed at the other binding site). **(F)** Close-up of GII.10 P domain 2'-FL complex structure (chewable) showing the binding interactions with 2'-FL shown in sticks and labeled. **(G)** Surface representation and closeup (right-side) of the GII.4 P domain dimer (chain A and B, light gray and dark gray, respectively) superimposed with 2'-FL (cyan sticks) and different HBGA types (colored accordingly): A-type (PDB ID: 4WZT, pink), B-type (PDB ID: 4OP7, grey), H2-type (PDB ID: 4WZK, brown),

Lewis-Y (PDB ID: 4WZE, magenta), Lewis-X (PDB ID: 4X0C, purple), and Lewis-B (PDB ID: 4OPO, lime). **(H)** The P domain is removed to show the orientation of 2'-FL with respect to HBGA H2-type, Lewis-Y, Lewis-X, and Lewis-B, A-type, and B-type.

## Materials and Methods

**Sequence analysis.** The full-length capsid amino acid sequences of GII.4c ([25](#)), GII.4-CHDC (ACT76142, CHDC-1974), GII.4-Syd (JX459908, Syd-2012), GII.8 (AF195848, Amsterdam), GII.10 (AF504671, Vietnam026), GII.14 (AY130761, M7), GII.17-CS-E1 (AY502009, CS-E1), GII.24 (KY225989, Loreto1972), GII.26 (KU306738, Leon4509), and GII.NA1 (NA: Not Assigned, MG495079, Loreto1257) ([2](#)) were aligned using Clustal Omega ([51](#)). These capsids had 64-91% amino acid identity and varying lengths, GII.8 (537 amino acids), GII.14 (536 amino acids), GII.17 (539 amino acids), GII.24 (542 amino acids), GII.26 (542 amino acids), and GII.NA1 (542 amino acids) ([2](#)).

**Norovirus P domain and VLP production.** The norovirus P domain gene of GII.4c, GII.8, GII.14, GII.17, GII.24, GII.26, and GII.NA1 were cloned and expressed as described ([6](#)). Briefly, the P domain was cloned into a modified expression vector (pMal-c2X) and transformed into *E. coli* BL21 cells, which were grown in LB medium at 37 °C. Expression was induced with 0.7 mM IPTG (OD<sub>600</sub> = 0.6) for 18 h at 22 °C. Cells were harvested by centrifugation and disrupted by sonication on ice. The His-tagged fusion-P domain protein was purified from a Ni-column (Qiagen) and digested with HRV-3C protease (Novagen) overnight at 4 °C. The cleaved P domain was separated on the Ni-column and dialyzed in gel filtration buffer (25 mM Tris-HCl (pH 7.6) and 300 mM NaCl) overnight at 4 °C. The P domain was further purified by size exclusion chromatography (SEC) using a AKTA Prime with a Superdex 75/200 column, concentrated to 2-4 mg/mL, and stored at 4 °C. The GII.4 and GII.10 VLPs were produced as described ([34](#)).

**Fc-NB26 design and production.** NB26 was expressed in *E. coli* WK6 cells as described ([33](#)). To generate Fc-NB26, the C-terminus of NB26 was designed to contain the pINFUSE-hIgG1-Fc1 sequence (pINFUSE-hIgG1-Fc1, InvivoGen), while the N- and C-terminus contained ATTB1 and ATTB2 sequences, respectively. The Fc-NB26 sequence was commercially synthesized (Invitrogen) for Gateway cloning (pDEST8) and expression in the insect cell baculovirus system. Briefly, bacmids were generated from the pDEST-Fc-NB26 plasmid, for transfection of Sf9 cells. After 5 days post transfection of Sf9 cells, the culture was centrifuged at 1057 × g for 10 min at 4 °C (to develop seed Fc-NB26 recombinant baculovirus). The Fc-NB26 seed virus was subsequently used to infect HighFive insect cells (Invitrogen). After 4-5 days post infection (dpi), the Fc-NB26 was separated from insect cells at 4,960 × g for 1 h at 4 °C. The Fc-NB26 containing supernatant was mixed 1:1 with Protein A IgG Binding Buffer (Pierce), incubated on the Protein A Agarose (Pierce), and then eluted using Protein A Elution Buffer (Pierce). Approximately 20 mg/L of purified Fc-NB26 was prepared and was stable at 4 °C for >6 months. Fc-NB26 expression was confirmed using SDS-PAGE and SEC, concentrated to 0.6 mg/mL, and stored at 4 °C.

**Cross-reactivity studies using ELISA.** The cross-reactivity of Fc-NB26 was determined using a direct ELISA as previously described with slight modifications ([3](#), [14](#)). Microtiter plates (MaxiSorp, ThermoFisher) were coated with 100 µL/well (10 µg/mL) of P domain overnight at 4 °C. Plates were washed three times with phosphate-buffered saline (PBS; pH 7.4) containing 0.1% Tween 20 (PBS-T) and subsequently blocked with 5% skimmed milk in PBS for 1 h at room temperature. Fc-NB26 was (1:1) serially diluted in PBS (starting at 1.2 µg/mL) and 100 µL/well applied to the washed microtiter plates and then incubated for 1 h at 37 °C.

The plates were washed and 100  $\mu$ L of 1:4,000 goat anti-human Fc-HRP Mab was added to each well (#31413, ThermoFisher). Plates were washed and then developed with 50  $\mu$ L of TMB (OptEIA TMB Substrate Reagent Set, BD) in the dark for 30 min at room temperature. Finally, the reaction was stopped with 25  $\mu$ L of 6% (v/v) HCl and absorption was measured at 450 nm ( $OD_{450}$ ). For this assay, a cutoff limit was set at  $OD_{450} > 0.18$ , which was  $\sim 3$  times the value of the PBS negative control ( $OD_{450} = 0.06$ ). A negative control rabbit haemorrhagic disease virus P domain showed no cross-reactivity with Fc-NB26 (data not shown).

**HMO 2'-FL inhibition studies using ELISA.** The GII.4 VLPs were prepared and purified as previously described (34) and analyzed in a surrogate HBGA blocking assay (13, 37). Briefly, Maxisorp 96-well plates were coated with 100  $\mu$ L per well of A-type saliva (13, 37) overnight at 4  $^{\circ}$ C. Plates were washed and blocked as described above. Two different types of 2'-FL were purchased online, 2'-FL powder (ASIN: B08J8DTMGK, Layer Origin, USA) and a 2'-FL chewable tablet (ASIN: B09RF982C6, MOMSTAMIN, Korea). The 2'-FL (tablet and powder forms) was serially diluted (from 500  $\mu$ g/mL) in PBS and added to 50  $\mu$ g/mL of GII.4 VLPs for 1 h at room temperature. Then, 100  $\mu$ L per well of 2'-FL+VLP mixture was added for 1 h at 37  $^{\circ}$ C. The plates were washed and 100  $\mu$ L of 1:20,000 Fc-NB85 (identical to Fc-NB26, except for Nanobody sequence) was added per well for 1 h at 37  $^{\circ}$ C. The plates were washed and 100  $\mu$ L per well of an anti-Fc-HRP antibody (#31413, ThermoFisher) (1:20,000) diluted in PBS-T-SM was added for 1 h at 37  $^{\circ}$ C. The plates were then processed as above. The  $OD_{450}$  value of the untreated VLPs was set as the reference value corresponding to 100% binding and the percentage of inhibition was calculated as  $(1 - (\text{treated VLP mean } OD_{450} / \text{mean reference } OD_{450})) \times 100$ . Triplicate experiments were performed with six repeats per 2'-FL concentration.

**Isothermal titration calorimeter (ITC) measurements.** A Nano ITC (TA instruments) with a cell volume of 170  $\mu$ L was used to determine the binding affinity of NB26 and Fc-NB26 to GII.10 and GII.4-Syd P domains. Each experiment was performed in duplicate, and heat of NB26 titration into PBS (pH 7.4) was subtracted for each trace. A concentration of 100  $\mu$ M of NB26 was titrated as 30 injections of 1.5  $\mu$ L every 200 seconds, into the cell containing between 10-12  $\mu$ M of P domain. For Fc-NB26, 30 injections of 30  $\mu$ M of Fc-NB26 were titrated into 3  $\mu$ M of P domain. The baseline was equilibrated for 600-900 seconds before the first injection. Statistics were performed using a paired Student's T-test with a confidence level of 95-99%.

**Crystallization of norovirus P domains.** P domains crystals were grown using the hanging drop method and the following mother solutions, GII.4c (0.2 M magnesium formate dihydrate and 20% w/v PEG3350), GII.8 (0.2 M sodium chloride, 0.1 M sodium potassium phosphate (pH 6.2) and 50% v/v PEG200), GII.14 (0.1 M bicine and 10% v/v MPD), GII.17 (0.2 M TMAO, 0.1 M Tris (pH 8.5), and 50% w/v PEG2000 MME), GII.24 (0.2 M lithium sulfate, 0.1 M Bis-Tris (pH 5.5), and 25% w/v PEG3350), GII.26 (0.1 M ammonium acetate, 0.1 M Bis-Tris (pH 5.5), and 17% w/v PEG10,000), and GII.NA1 (0.2 M magnesium chloride hexahydrate, 0.1 M Tris (pH 7.0), and 10% w/v PEG8000) for 6-10 days at 18  $^{\circ}$ C. Prior to data collection, crystals were transferred to a cryoprotectant containing the mother solution in 30% ethylene glycol, followed by flash freezing in liquid nitrogen. For the GII.4c P domain HBGA complexes and GII.4-Syd and GII.10 2'-FL complexes, we either soaked a 60-molar excess of HBGA or 2'-FL into pre-made crystals and/or co-crystallized, respectively (6, 9, 37). Prior to data collection, crystals were transferred to a cryoprotectant containing the mother liquor, 30% ethylene glycol, and 30-60-molar excess of HBGA or 2'-FL.



**Data collection, structure solution, and refinement.** X-ray diffraction data were collected at MX1 and MX2 beamlines at the Australian Synchrotron, Australia and processed with XDS or AIMLESS (9, 40). Structures were solved by molecular replacement in PHASER *Phaser-MR* (52) using either GII.4-Syd (PDB ID: 4OOS) or GII.10 (PDB ID: 3ONU) P domains as search models. Structures were refined in multiple rounds of manual model building in COOT (53) and PHENIX (54). Structures were validated with *Procheck* (55) and *Molprobity* (56). Protein interactions were analyzed using PyMOL Molecular Graphics System, Version 2.1 Schrödinger, LLC (57). Atomic coordinates and structure factors are deposited in the Protein Databank (Tables S1, S2, and S3).

**Analysis of GII.4 capsid sequence conservation.** Amino acid sequence conservation was analyzed for GII.4 variants using an alignment over 2000 GII.4 capsid sequences. Residue conservation was computed using the AL2CO server with a Henikoff-Henikoff sequence weighting scheme, normalized conservation values, and entropy-based conservation calculation (58). The computed residue conservation scores were mapped and colored white (highly variable) to deep purple (highly conserved) onto the surface of the unbound GII.4-Syd (PDB ID: 4OOS) structure using AL2CO (58) and a PyMOL script. Binding interfaces and interactions were analyzed using *PDBePISA* online server (<https://www.ebi.ac.uk/pdbe/pisa/>) (59) and PyMOL (version 1.2), with hydrogen bond distances ~2.36-3.88 Å and electrostatic distances ~2.56-3.89 Å. Water-mediated interactions were excluded from the analysis.

**HIE culture system and NB26 and Fc-NB26 inhibition studies.** Secretor-positive jejunal HIE culture (J2) and Noggin producing cell lines were provided by Baylor College of Medicine, USA and processed as described with slight modifications (41) using a positive GII.4 norovirus stool sample (41). Briefly, HIE were trypsinized and grown as 2D monolayers in a collagen coated 96 well plates. After one day, the complete media growth factor positive (CMGF+) media was changed to differentiation media for five days. Monolayers were pretreated with 500 µM glycochenodeoxycholic acid (GCDCA) for two days before infection experiments. Confluent monolayers were washed once with ice cold CMGF- and incubated for 1 h at 37 °C with diluted stool samples. After infection, monolayers were washed twice with ice cold PBS and incubated in differentiation media supplemented with 500 µM GCDCA or 500 µM GCDCA and 1% human bile. Samples were frozen at 0 days post infection (dpi), i.e., 1 h after virus attachment and 3 dpi. For inhibition experiments, diluted stool samples were preincubated with serially diluted NB26 or Fc-NB26 for 1 h at 37 °C. The concentrations of NB26 and Fc-NB26 were calculated using a Nanodrop (ThermoFisher). For Fc-NB26, the concentration was calculated using a extinction coefficient at 280 nm for the *Fc-NB26 amino acid sequence* of 1.492 (60). Isotype IgG (anti-myosin heavy chain antibody, Abcam) at 200 µg/mL was used as a negative control. Confluent monolayers were washed once with ice cold CMGF- and incubated for 1 h at 37 °C with diluted stool samples. After infection, monolayers were washed twice with ice cold PBS and incubated in differentiation media. Plates were frozen at 0 dpi and 3 dpi. Viral RNA was extracted using RNAeasy mini kit (Qiagen) or phenol/chloroform extraction with RiboZol according to manufacturer instructions. Genome copy levels were measured using qScript XLT One-step RT-qPCR ToughMix reagent with ROX (Quanta Biosciences) using COG2R/QNIF2D primer pair, and probe QNIFS as described previously. All experiments were performed three times with technical quadruplicates. A standard curve based on human norovirus RNA transcript was used to quantitate viral genome equivalents. Percent inhibition in viral genome equivalents relative to the IgG control was determined. Differences were considered significant when P value < 0.05. The IC<sub>50</sub> values were analyzed using Microsoft Excel and GraphPad Prism (version 10.0).

**Negative stain electron microscopy of untreated and Nanobody treated VLPs.** Untreated GII.10 VLPs were diluted to 0.03 mg/mL in TBS (10 mM Tris HCl and 150 mM NaCl (pH 7.5)) and stained on carbon-coated Ted Pella grids using 2% uranyl formate. For the complexes, GII.10 VLPs were treated by mixing 1.0 mg/mL GII.10 VLP with 1.0 mg/mL of NB26 or Fc-NB26 for 1 h at room temperature. The mixtures were then diluted to 0.05 mg/mL with distilled water before staining on carbon-coated Ted Pella grids using 2% uranyl formate. Each grid was analyzed on a Talos (L120C) TEM and images collected at 92,000 × magnification.

### Supplementary Figures

**Figure S1. Amino acid alignment of 15 GII genotypes used in this study.** The P1-1, P2, and P1-2 subdomains are marked with a solid bar (in green for P1 and blue for P2). Highly conserved residues are indicated with an “\*”. The location of Loops A, B, C, and D is shaded pink. Two residues, arginine (R) and aspartic acid (D), whose side chains bind fucose moiety of HBGAs are highly conserved and boxed in grey. The NB26 binding epitope based on GII.10 P domain NB26 complex (PDB ID: 5O04) was predicted for the other genotypes using PyMOL and *PDBePISA* online server.

**Figure S2. Structural alignment of 15 GII genotype P domains.** Structures of fifteen aligned P domains are shown individually with the same orientation and size to show the extensive loop variations on the side (A) and top (B) views. The P dimers are shown in blue (P1), light blue (P2), pink (P1) and salmon (P2). Black arrows and pink boxes indicate the position of the extended loops. The H2-type (green sticks) from the GII.4 Saga P domain H2-type complex structure (PDB ID: 4WZK) was superimposed to show the HBGA pocket, with the Saga P domain removed.

**Figure S3. Representative simulated annealing difference omit maps.** The saccharides present in GII.4c P domain H2-type, GII.4-Syd P domain 2'-FL (powder) complex, GII.10 P domain 2'-FL (powder), GII.10 P domain 2'-FL (tablet) complex structures are shown and labeled fucose (Fuc), galactose (Gal), or glucose (Glc). The omit map (orange) is contoured between 2.5-2.0  $\sigma$ . The H2-type is a trisaccharide composed of an  $\alpha$ -L-fucose-(1-2)- $\beta$ -D-galactose-(3-1)-2-N-acetyl- $\alpha$ -D-galactosamine (only underlined portion was fitted into structure). The 2'-FL is a trisaccharide composed of an  $\alpha$ -L-fucose-(1-2)- $\beta$ -D-galactose-(1-4)- $\alpha$ -D-glucose.

**Figure S4. Summary of GII P domains.** Fifteen P domains superimposed with the H2-type (green sticks) from the GII.4 Saga P domain H2-type complex structure (PDB ID: 4WZK) to show the HBGA pocket (Saga P domain removed). Structures are shown from top (top panel) and side (bottom panel) views. Two highly conserved side chain residues in all GII genotypes that interact with the fucose moieties found in HBGAs and HMO are shown as sticks and labeled.

**Figure S5. Design and development of Fc-NB26.** (A) Amino acid sequence of NB26 (cyan) fused to a human IgG hinge (red) followed by human IgG Fc (green). (B) SDS-PAGE of Fc-NB26 (arrow showing Fc-NB26 monomer of 38.4 kDa) and NB26 (arrow showing NB26 of 15 kDa). (C) SEC graph of Fc-NB26 using a Superdex 75/200 column (D) SEC of NB26 using a Superdex 75/200 column.

**Figure S6. Amino acid alignment of NB26 and M4.** Amino acid sequence alignment of NB26 and M4, showing residues R26 and R100, respectively. The CDRs for NB26 (CDR1, 26-33;

CDR2, 52-55; and CDR3, 98-108) and M4 (CDR1, 26-33; CDR2, 52-55, and CDR3, 98-108) are labeled and underlined.

**Figure S7. Thermodynamic properties of NB26 and Fc-NB26 binding to P domains using ITC.** NB26 or Fc-NB26 was titrated into (A) GII.10 P domain or (B) GII.4-Syd P domain. Examples of the titration (upper) of NB26 or Fc-NB26 to P domains are shown. The binding isotherm was calculated using a single binding site model (lower). (C) Constants K (binding constant in  $M^{-1}$ ), dH (heat change in cal/mol), dS (entropy change in cal/mol/deg), and dG (change in free energy in cal/mol) are shown with standard deviations. Fc-NB26 has significantly higher affinity (>100 fold higher) to these P domains than NB26 (Student's T-test, P value < 0.05).

**Table S1. Data collection and refinement statistics for GII.8, GII.14, GII.17, GII.24, GII.26, and GII.NA1 P domains.**

**Table S2. Amino acid analysis of GII P domain X-ray crystal structures, where the P domain is further subdivided into P1-1, P2, and P1-2 subdomains.**

**Table S3. Data collection and refinement statistics for unbound GII.4c P domain and GII.4c P domain H2-type complex.**

**Table S4. Data collection and refinement statistics for GII.4 P domain 2'-FL and GII.10 P domain 2'-FL complexes.**

## References

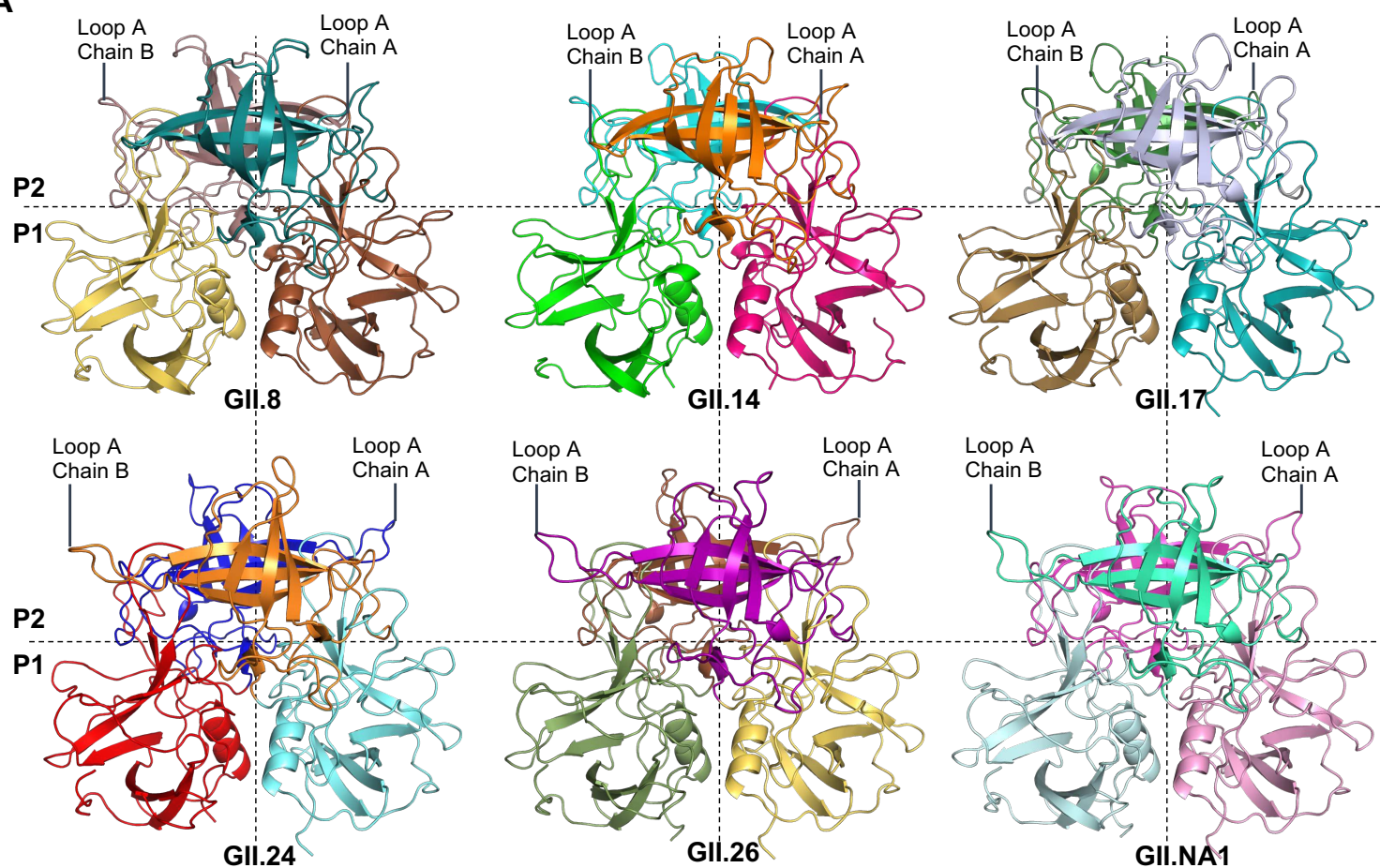
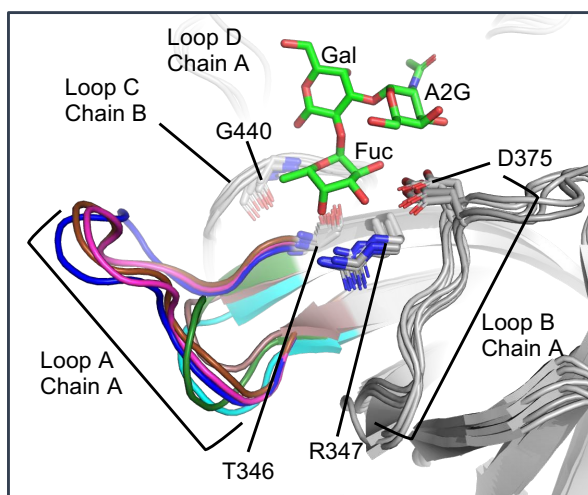
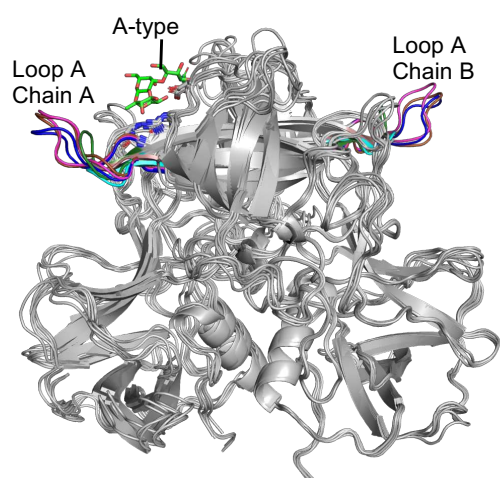
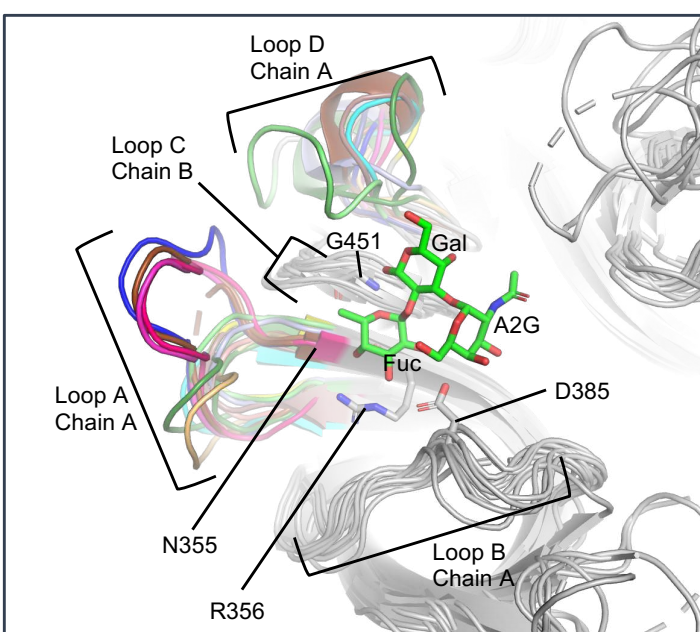
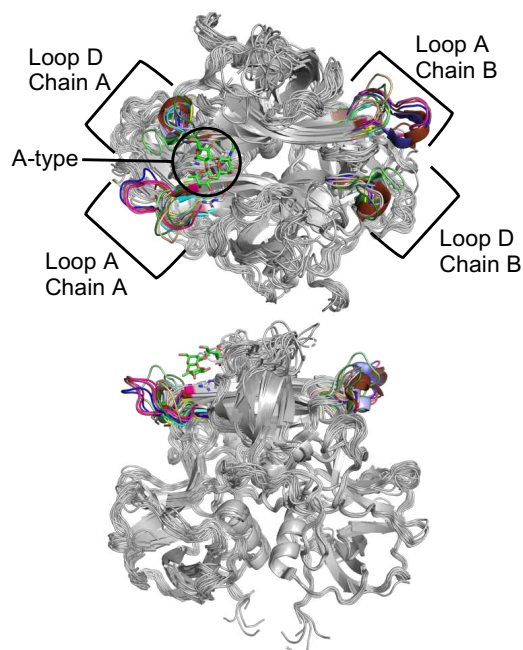
1. A. J. H. Sharia M Ahmed, Anne E Robinson, Linda Verhoef, Prasanna Premkumar, Umesh D Parashar, Marion Koopmans, Benjamin A Lopman, Global prevalence of norovirus in cases of gastroenteritis: a systematic review and meta-analysis. *The Lancet infectious diseases* **14**, 725-730 (2014).
2. P. Chhabra *et al.*, Corrigendum: Updated classification of norovirus genogroups and genotypes. *The Journal of general virology* **101**, 893 (2020).
3. G. S. Hansman *et al.*, Genetic and antigenic diversity among noroviruses. *The Journal of general virology* **87**, 909-919 (2006).
4. B. V. Prasad *et al.*, X-ray crystallographic structure of the Norwalk virus capsid. *Science* **286**, 287-290 (1999).
5. T. Kilic, A. Koromyslova, G. S. Hansman, Structural Basis for Human Norovirus Capsid Binding to Bile Acids. *Journal of virology* **93**, (2019).
6. G. S. Hansman *et al.*, Crystal structures of GII.10 and GII.12 norovirus protruding domains in complex with histo-blood group antigens reveal details for a potential site of vulnerability. *Journal of virology* **85**, 6687-6701 (2011).
7. P. R. Harrington, L. Lindesmith, B. Yount, C. L. Moe, R. S. Baric, Binding of Norwalk virus-like particles to ABH histo-blood group antigens is blocked by antisera from infected human volunteers or experimentally vaccinated mice. *Journal of virology* **76**, 12335-12343 (2002).
8. K. Ettayebi *et al.*, Replication of human noroviruses in stem cell-derived human enteroids. *Science* **353**, 1387-1393 (2016).
9. B. K. Singh, M. M. Leuthold, G. S. Hansman, Human noroviruses' fondness for histo-blood group antigens. *Journal of virology* **89**, 2024-2040 (2015).
10. X. Cong *et al.*, GII.13/21 Noroviruses Recognize Glycans with a Terminal  $\beta$ -Galactose via an Unconventional Glycan Binding Site. *Journal of virology* **93**, (2019).

11. Y. Qian *et al.*, Structural Adaptations of Norovirus GII.17/13/21 Lineage through Two Distinct Evolutionary Paths. *Journal of virology* **93**, (2019).
12. A. Kocak, HBGA binding modes and selectivity in noroviruses upon mutation: a docking and molecular dynamics study. *Journal of molecular modeling* **25**, 369 (2019).
13. A. Koromyslova, S. Tripathi, V. Morozov, H. Schrotten, G. S. Hansman, Human norovirus inhibition by a human milk oligosaccharide. *Virology* **508**, 81-89 (2017).
14. B. K. Singh, M. M. Leuthold, G. S. Hansman, Structural Constraints on Human Norovirus Binding to Histo-Blood Group Antigens. *mSphere* **1**, e00049-00016 (2016).
15. W. Liu *et al.*, A Unique Human Norovirus Lineage with a Distinct HBGA Binding Interface. *PLoS pathogens* **11**, e1005025 (2015).
16. S. Shanker *et al.*, Structural analysis of histo-blood group antigen binding specificity in a norovirus GII.4 epidemic variant: implications for epochal evolution. *Journal of virology* **85**, 8635-8645 (2011).
17. S. Cao *et al.*, Structural basis for the recognition of blood group trisaccharides by norovirus. *Journal of virology* **81**, 5949-5957 (2007).
18. V. Blazevic, S. Lappalainen, K. Nurminen, L. Huhti, T. Vesikari, Norovirus VLPs and rotavirus VP6 protein as combined vaccine for childhood gastroenteritis. *Vaccine* **29**, 8126-8133 (2011).
19. M. Malm, K. Tamminen, T. Vesikari, V. Blazevic, Norovirus-Specific Memory T Cell Responses in Adult Human Donors. *Frontiers in microbiology* **7**, 1570 (2016).
20. L. Kim *et al.*, Safety and immunogenicity of an oral tablet norovirus vaccine, a phase I randomized, placebo-controlled trial. *JCI Insight* **3**, e121077 (2018).
21. G. Leroux-Roels *et al.*, Safety and Immunogenicity of Different Formulations of Norovirus Vaccine Candidate in Healthy Adults: A Randomized, Controlled, Double-Blind Clinical Trial. *J Infect Dis* **217**, 597-607 (2018).
22. D. I. Bernstein *et al.*, Norovirus vaccine against experimental human GII.4 virus illness: a challenge study in healthy adults. *J Infect Dis* **211**, 870-878 (2015).
23. G. I. Parra *et al.*, Immunogenicity and specificity of norovirus Consensus GII.4 virus-like particles in monovalent and bivalent vaccine formulations. *Vaccine* **30**, 3580-3586 (2012).
24. L. C. Lindesmith *et al.*, Broad blockade antibody responses in human volunteers after immunization with a multivalent norovirus VLP candidate vaccine: immunological analyses from a phase I clinical trial. *PLoS medicine* **12**, e1001807 (2015).
25. G. I. Parra *et al.*, Immunogenicity and specificity of norovirus Consensus GII.4 virus-like particles in monovalent and bivalent vaccine formulations. *Vaccine* **30**, 3580-3586 (2012).
26. C. P. Mattison, C. V. Cardemil, A. J. Hall, Progress on norovirus vaccine research: public health considerations and future directions. *Expert review of vaccines*, 1-12 (2018).
27. L. Garaicoechea *et al.*, Llama nanoantibodies with therapeutic potential against human norovirus diarrhea. *PloS one* **10**, e0133665 (2015).
28. Y. Yuki *et al.*, Lactobacilli as a Vector for Delivery of Nanobodies against Norovirus Infection. *Pharmaceutics* **15**, (2022).
29. Y. Yuki *et al.*, A Heterodimeric Antibody Fragment for Passive Immunotherapy Against Norovirus Infection. *The Journal of infectious diseases* **222**, 470-478 (2020).
30. J. M. Devant, G. S. Hansman, Structural heterogeneity of a human norovirus vaccine candidate. *Virology* **553**, 23-34 (2021).
31. A. D. Koromyslova *et al.*, Nanobody-Mediated Neutralization Reveals an Achilles Heel for Norovirus. *Journal of virology* **94**, (2020).

32. K. Ruoff *et al.*, Structural Basis of Nanobodies Targeting the Prototype Norovirus. *Journal of virology* **93**, e02005-02018 (2019).
33. A. D. Koromyslova, G. S. Hansman, Nanobodies targeting norovirus capsid reveal functional epitopes and potential mechanisms of neutralization. *PLoS pathogens* **13**, e1006636 (2017).
34. A. D. Koromyslova, G. S. Hansman, Nanobody binding to a conserved epitope promotes norovirus particle disassembly. *Journal of virology* **89**, 2718-2730 (2015).
35. W. Salmen *et al.*, A single nanobody neutralizes multiple epochally evolving human noroviruses by modulating capsid plasticity. *Nature communications* **14**, 6516 (2023).
36. I. Jovcevska, S. Muyldermans, The Therapeutic Potential of Nanobodies. *BioDrugs* **34**, 11-26 (2020).
37. S. Weichert *et al.*, Structural Basis for Norovirus Inhibition by Human Milk Oligosaccharides. *Journal of virology* **90**, 4843-4848 (2016).
38. B. K. Singh, A. Koromyslova, L. Hefele, C. G rth, G. S. Hansman, Structural Evolution of the Emerging 2014-2015 GII.17 Noroviruses. *Journal of virology* **90**, 2710-2715 (2015).
39. A. D. Koromyslova, M. M. Leuthold, M. W. Bowler, G. S. Hansman, The sweet quartet: Binding of fucose to the norovirus capsid. *Virology* **483**, 203-208 (2015).
40. G. Kher *et al.*, Direct Blockade of the Norovirus Histo-Blood Group Antigen Binding Pocket by Nanobodies. *Journal of virology*, e0183322 (2023).
41. A. D. Koromyslova, V. A. Morozov, L. Hefele, G. S. Hansman, Human Norovirus Neutralized by a Monoclonal Antibody Targeting the Histo-Blood Group Antigen Pocket. *Journal of virology* **93**, (2019).
42. G. Ye *et al.*, Discovery of Nanosota-2, -3, and -4 as super potent and broad-spectrum therapeutic nanobody candidates against COVID-19. *Journal of virology*, e0144823 (2023).
43. J. Ettich *et al.*, A Hybrid Soluble gp130/Spike-Nanobody Fusion Protein Simultaneously Blocks Interleukin-6 trans-Signaling and Cellular Infection with SARS-CoV-2. *Journal of virology* **96**, e0162221 (2022).
44. H. Ma *et al.*, Potent Neutralization of SARS-CoV-2 by Hetero-bivalent Alpaca Nanobodies Targeting the Spike Receptor-Binding Domain. *Journal of virology*, (2021).
45. T. Li *et al.*, A synthetic nanobody targeting RBD protects hamsters from SARS-CoV-2 infection. *Nature communications* **12**, 4635 (2021).
46. V. Bobkov *et al.*, Nanobody-Fc constructs targeting chemokine receptor CXCR4 potentially inhibit signaling and CXCR4-mediated HIV-entry and induce antibody effector functions. *Biochem Pharmacol* **158**, 413-424 (2018).
47. H. Schroten, F. G. Hanisch, G. S. Hansman, Human norovirus interactions with histo-blood group antigens and human milk oligosaccharides. *Journal of virology*, (2016).
48. L. C. Lindesmith *et al.*, Sera Antibody Repertoire Analyses Reveal Mechanisms of Broad and Pandemic Strain Neutralizing Responses after Human Norovirus Vaccination. *Immunity* **50**, 1530-1541.e1538 (2019).
49. G. Alvarado *et al.*, Broadly cross-reactive human antibodies that inhibit genogroup I and II noroviruses. *Nature communications* **12**, 4320 (2021).
50. B. Hegar *et al.*, The Role of Two Human Milk Oligosaccharides, 2'-Fucosyllactose and Lacto-N-Neotetraose, in Infant Nutrition. *Pediatric gastroenterology, hepatology & nutrition* **22**, 330-340 (2019).
51. F. Sievers *et al.*, Fast, scalable generation of high-quality protein multiple sequence alignments using Clustal Omega. *Mol Syst Biol* **7**, 539 (2011).

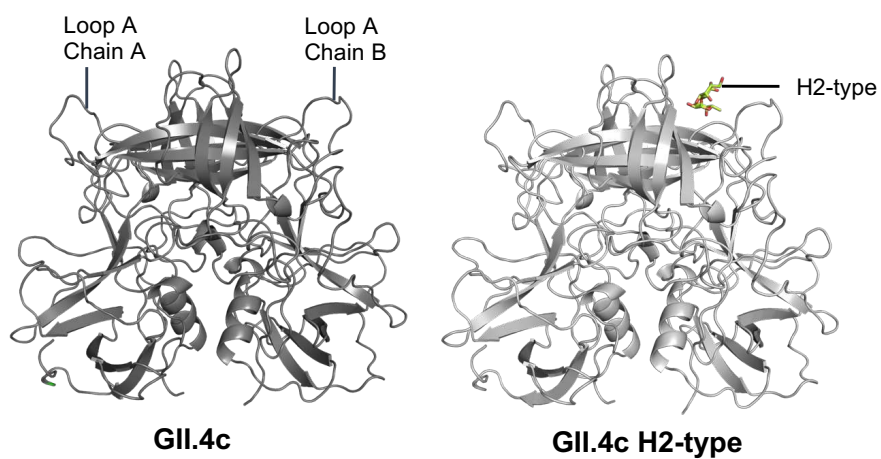
52. G.-K. R. McCoy AJ, Adams PD, Winn MD, Storoni LC, Read RJ. , Phaser crystallographic software. *Journal of Applied Crystallography*. **40**, 658-674 (2007).
53. L. B. Emsley P, Scott WG, Cowtan K., Features and development of Coot. *Acta Crystallographica Section D: Biological Crystallography*. **66**, 486-501 (2010).
54. P. D. Adams *et al.*, PHENIX: a comprehensive Python-based system for macromolecular structure solution. *Acta Crystallographica Section D* **66**, 213-221 (2010).
55. M. M. Morris AL, Hutchinson EG, Thornton JM., Stereochemical quality of protein structure coordinates. *Proteins* **12**, 345-364 (1992).
56. A. W. Chen VB, Headd JJ, Keedy DA, Immormino RM, Kapral GJ, Murray LW, Richardson JS & Richardson DC, MolProbity: all-atom structure validation for macromolecular crystallography. *Acta Crystallographica Section D* **D66**, 12-21 (2010).
57. Schrodinger, LLC. (2015).
58. J. Pei, N. V. Grishin, AL2CO: calculation of positional conservation in a protein sequence alignment. *Bioinformatics* **17**, 700-712 (2001).
59. E. Krissinel, K. Henrick, Inference of macromolecular assemblies from crystalline state. *Journal of molecular biology* **372**, 774-797 (2007).
60. M. R. Wilkins *et al.*, Protein identification and analysis tools in the ExPASy server. *Methods in molecular biology* **112**, 531-552 (1999).



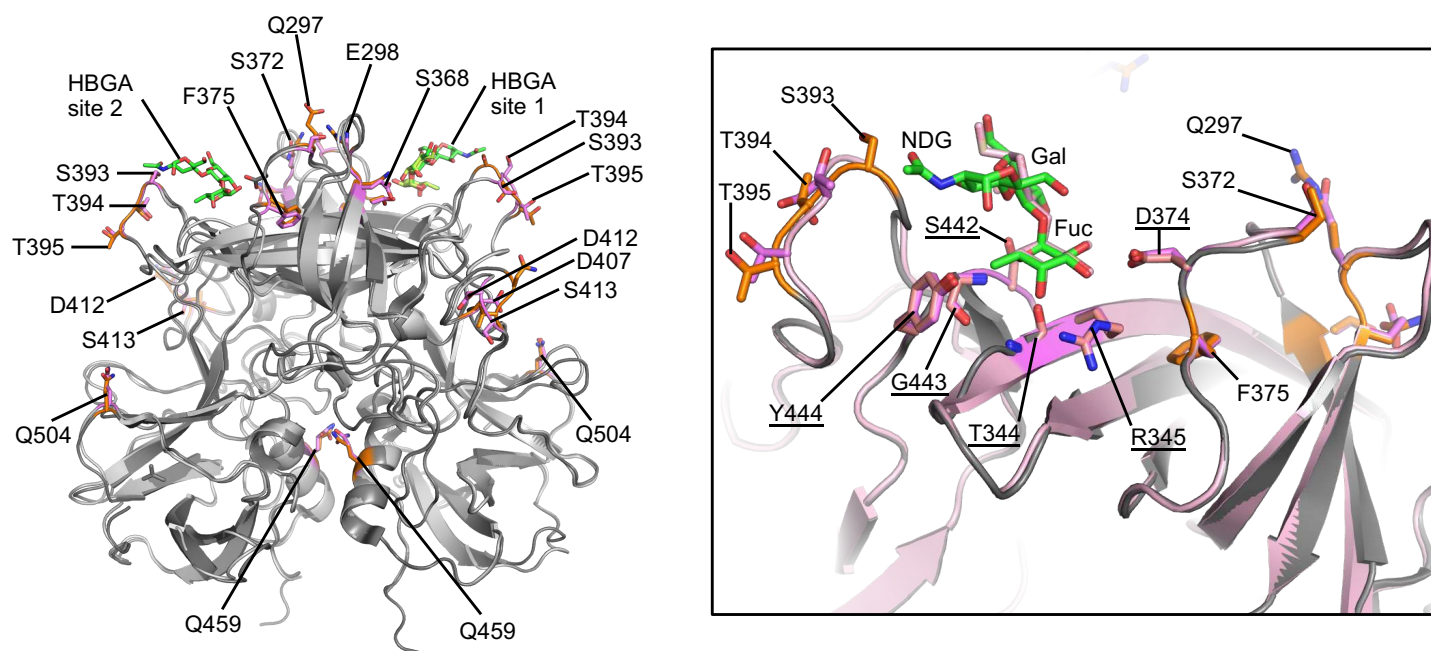
**Figure 1****A****B****C**



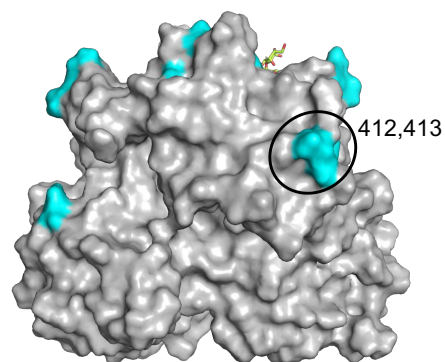
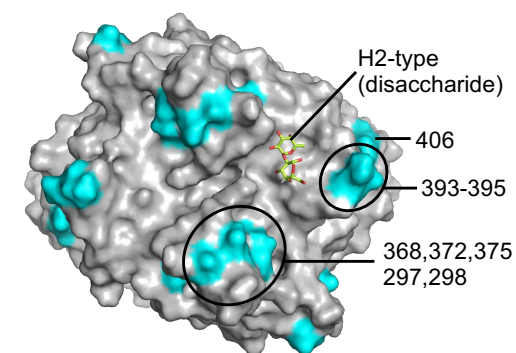
A



B

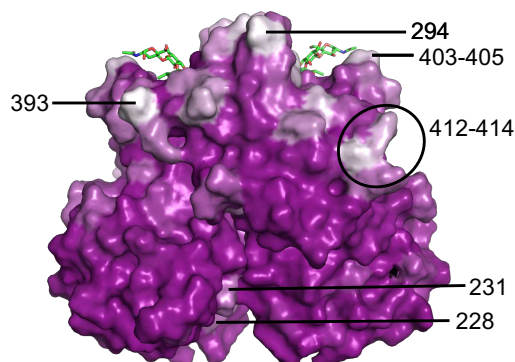
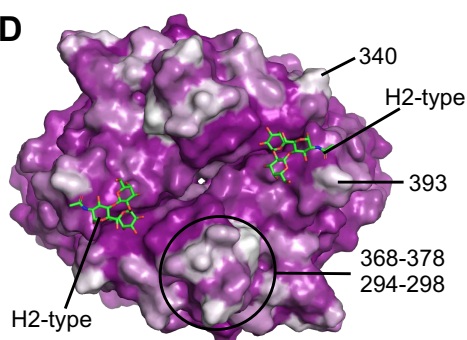


C



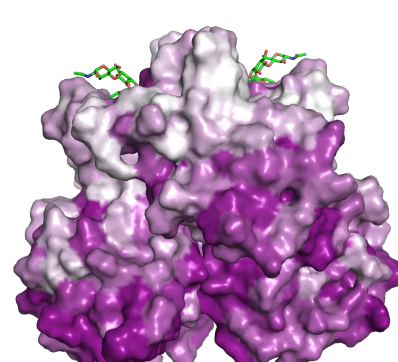
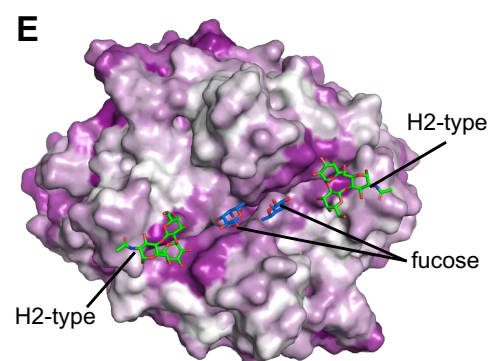
**Engineered GII.4c**  
**N=3 sequences**

D



**GII.4 natural selection**  
**N=2000 sequences**

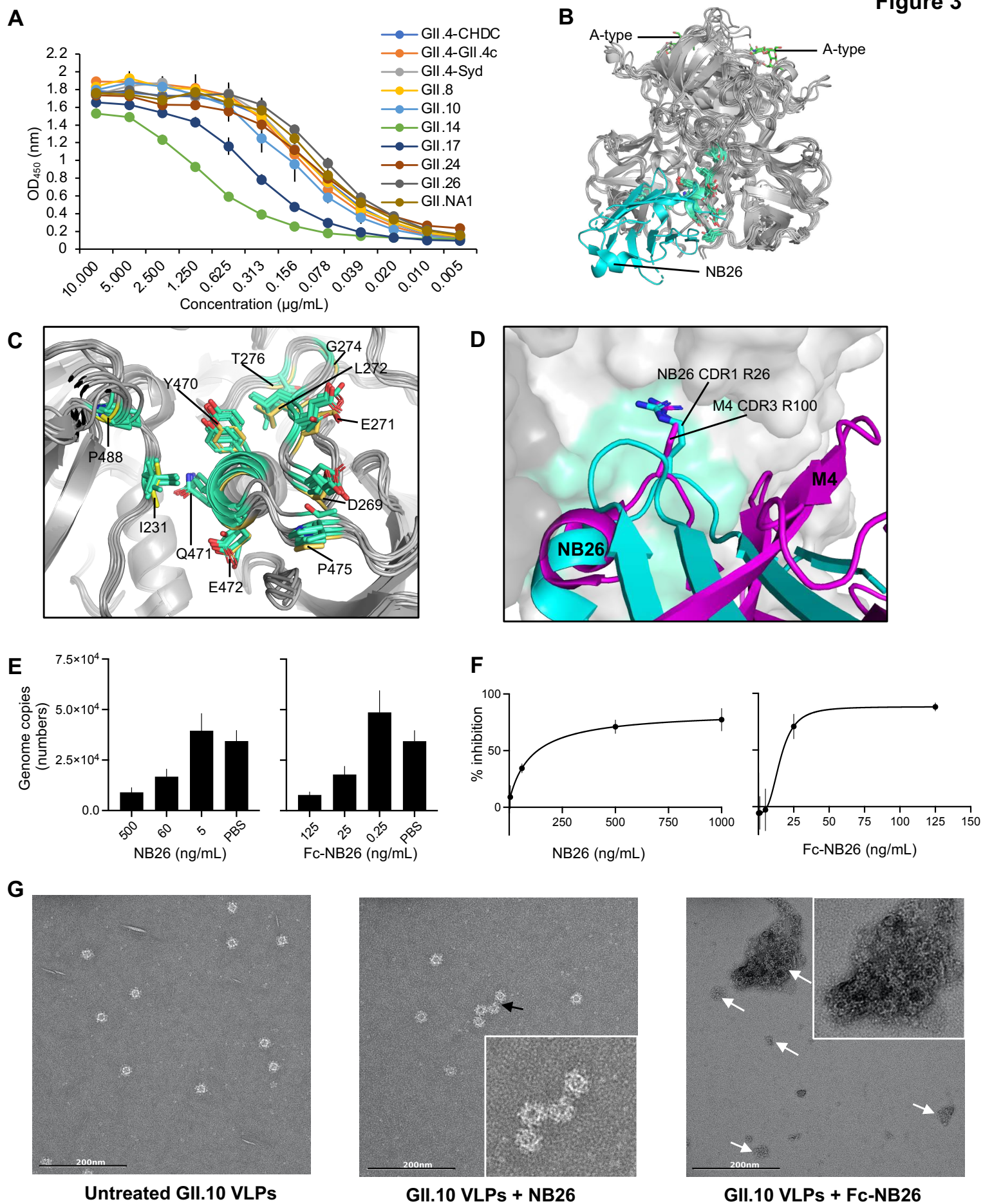
E



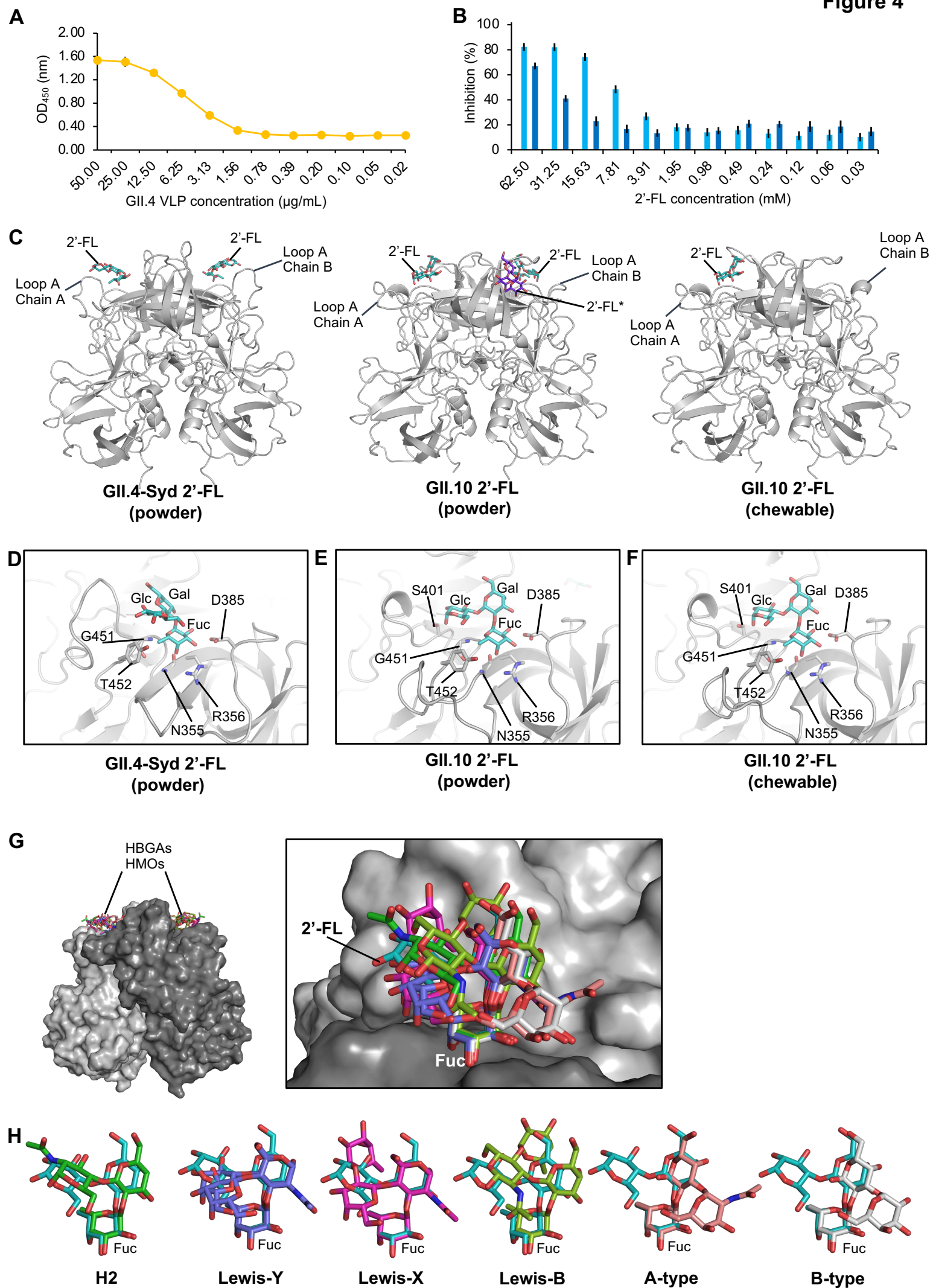
**GII natural selection**  
**N=29 sequences**



**Figure 3**



**Figure 4**



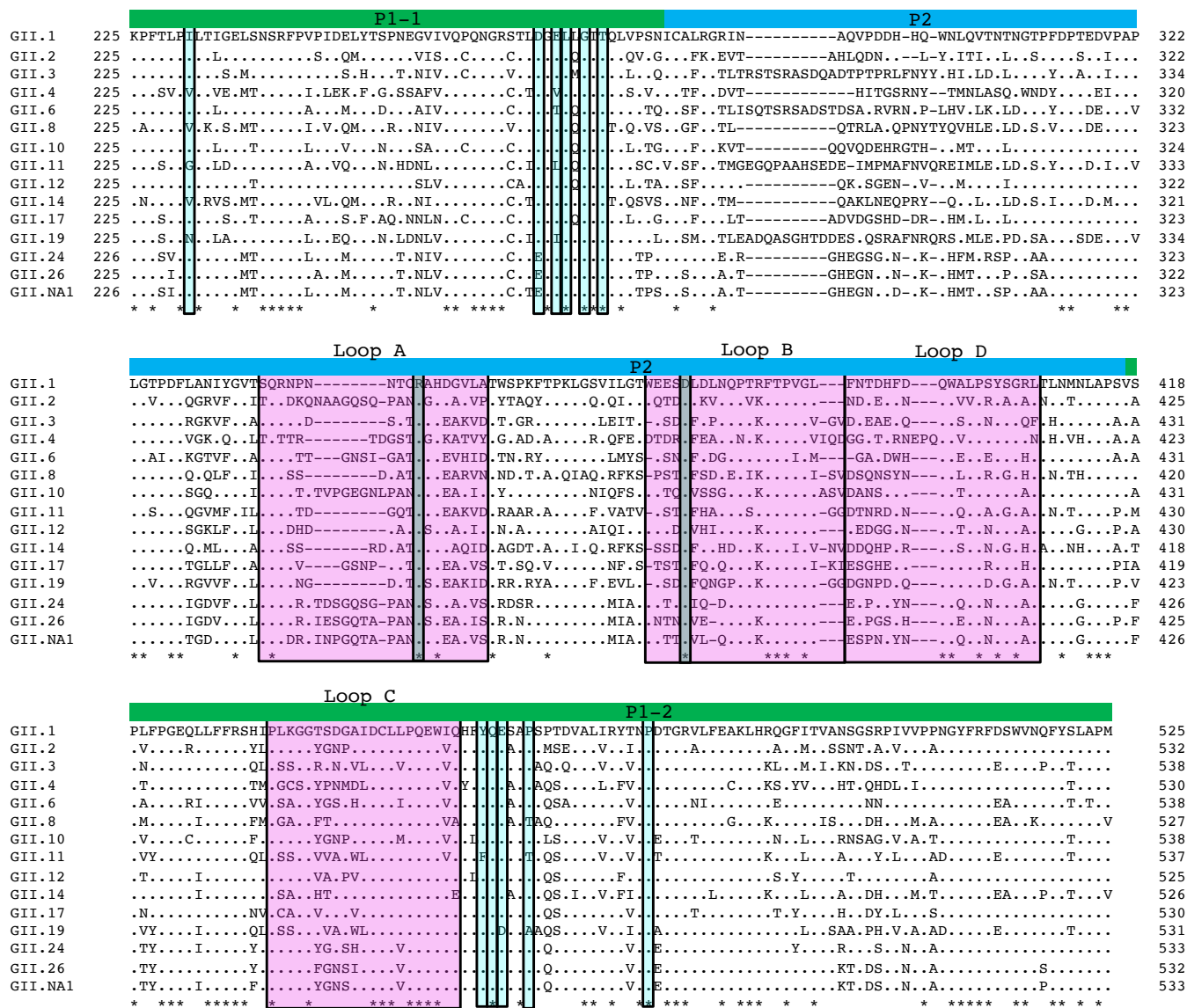


**Figure S1. Amino acid alignment of 15 GII genotypes used in this study.** The P1-1, P2, and P1-2 subdomains are marked with a solid bar (in green for P1 and blue for P2). Highly conserved residues are indicated with an “\*”. The location of Loops A, B, C, and D is shaded pink. Two residues, arginine (R) and aspartic acid (D), whose side chains bind fucose moiety of HBGAs are highly conserved and boxed in grey. The NB26 binding epitope based on GII.10 P domain NB26 complex (PDB ID: 5O04) was predicted for the other genotypes using PyMOL and *PDBePISA* online server.



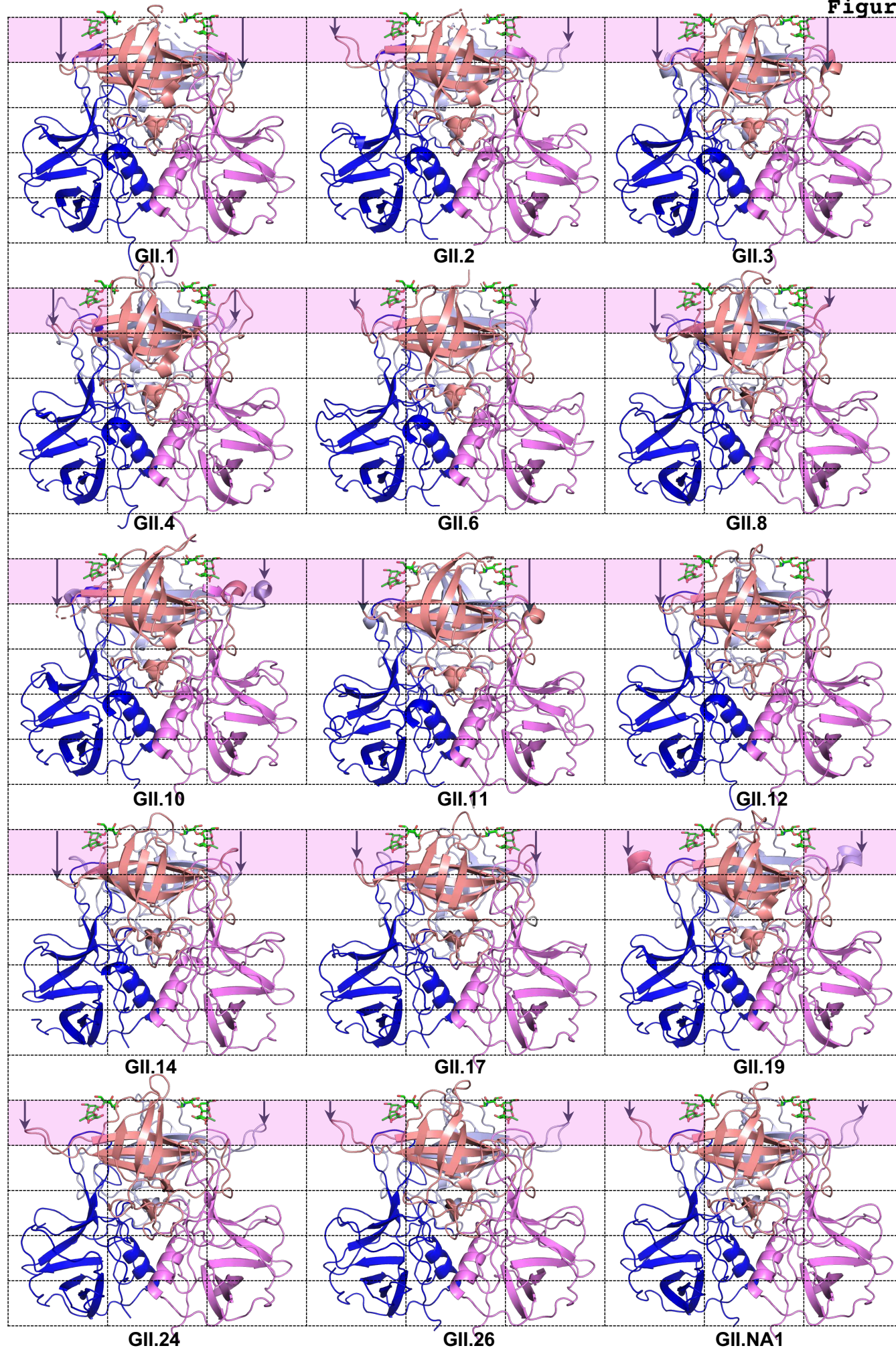


**Figure S2. Structural alignment of 15 GII genotype P domains.** Structures of fifteen aligned P domains are shown individually with the same orientation and size to show the extensive loop variations on the side (A) and top (B) views. The P dimers are shown in blue (P1), light blue (P2), pink (P1) and salmon (P2). Black arrows and pink boxes indicate the position of the extended loops. The H2-type (green sticks) from the GII.4 Saga P domain H2-type complex structure (PDB ID: 4WZK) was superimposed to show the HBGA pocket, with the Saga P domain removed.



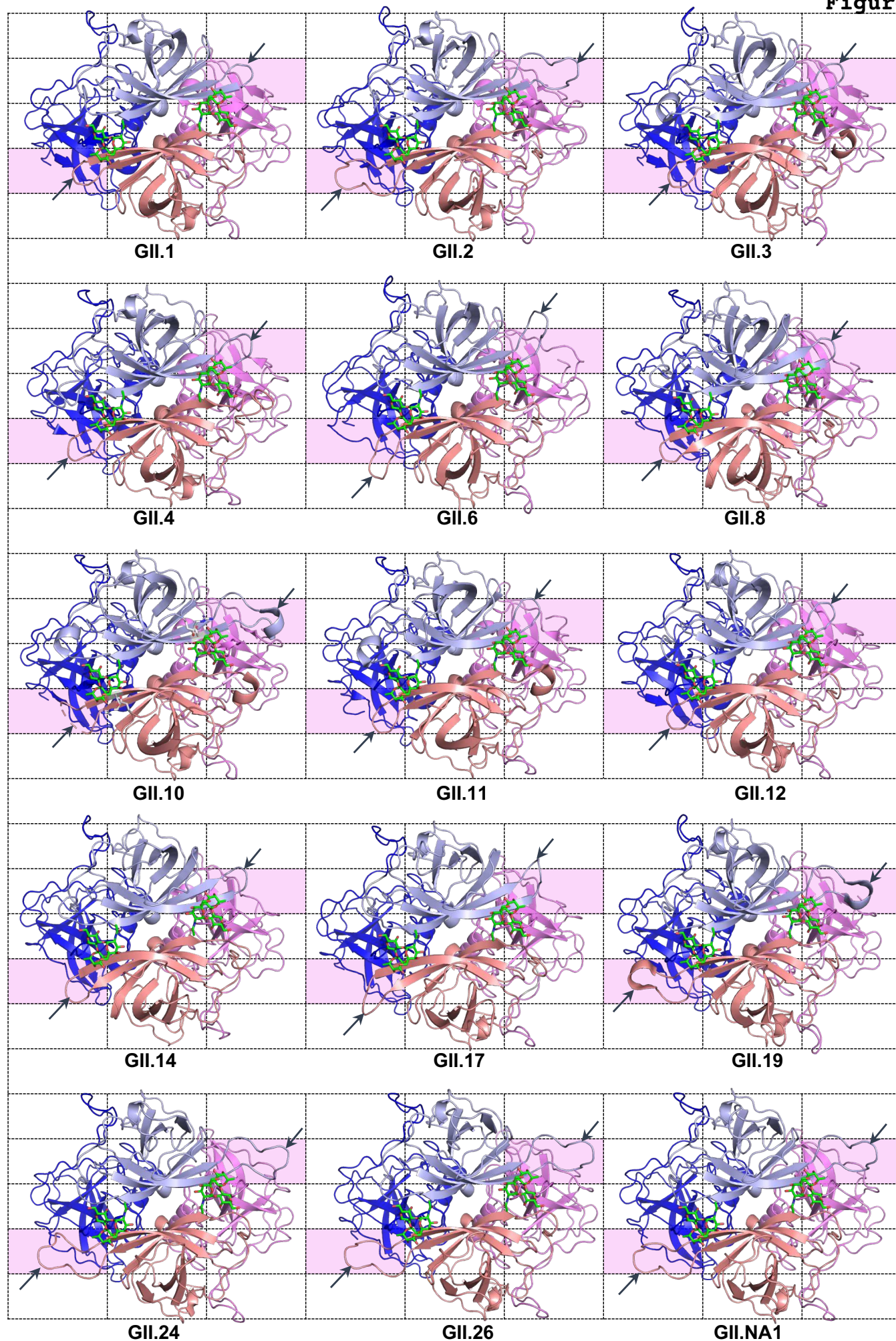
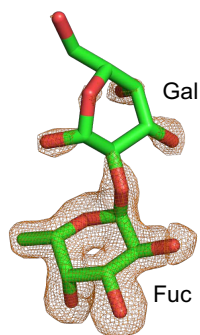
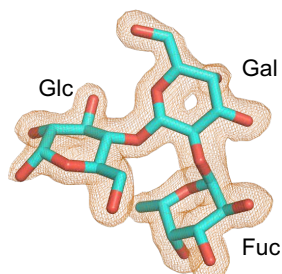


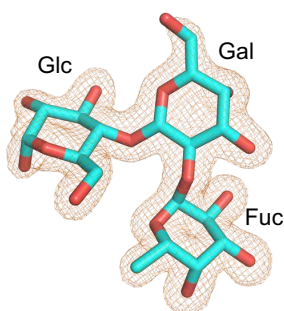
**Figure S2. Structural alignment of 15 GII genotype P domains.** Structures of fifteen aligned P domains are shown individually with the same orientation and size to show the extensive loop variations on the side (A) and top (B) views. The P dimers are shown in blue (P1), light blue (P2), pink (P1) and salmon (P2). Black arrows and pink boxes indicate the position of the extended loops. The H2-type (green sticks) from the GII.4 Saga P domain H2-type complex structure (PDB ID: 4WZK) was superimposed to show the HBGA pocket, with the Saga P domain removed.



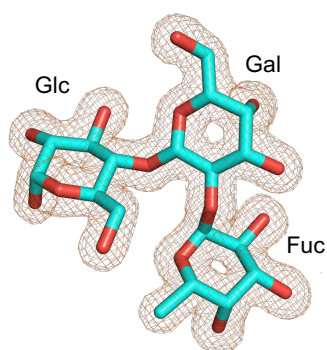
**H2-type (missing galactosamine)  
GII.4c P domain**



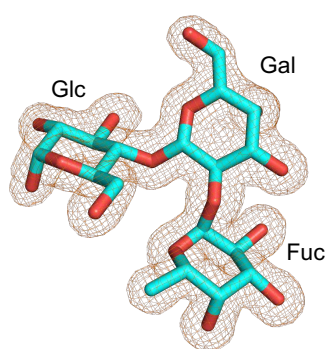
**2'-FL (powder)  
GII.4-Syd P domain**



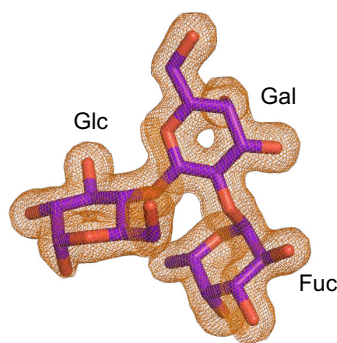
**2'-FL (tablet)  
GII.10 P domain**



**2'-FL site 1 (powder)  
GII.10 P domain**



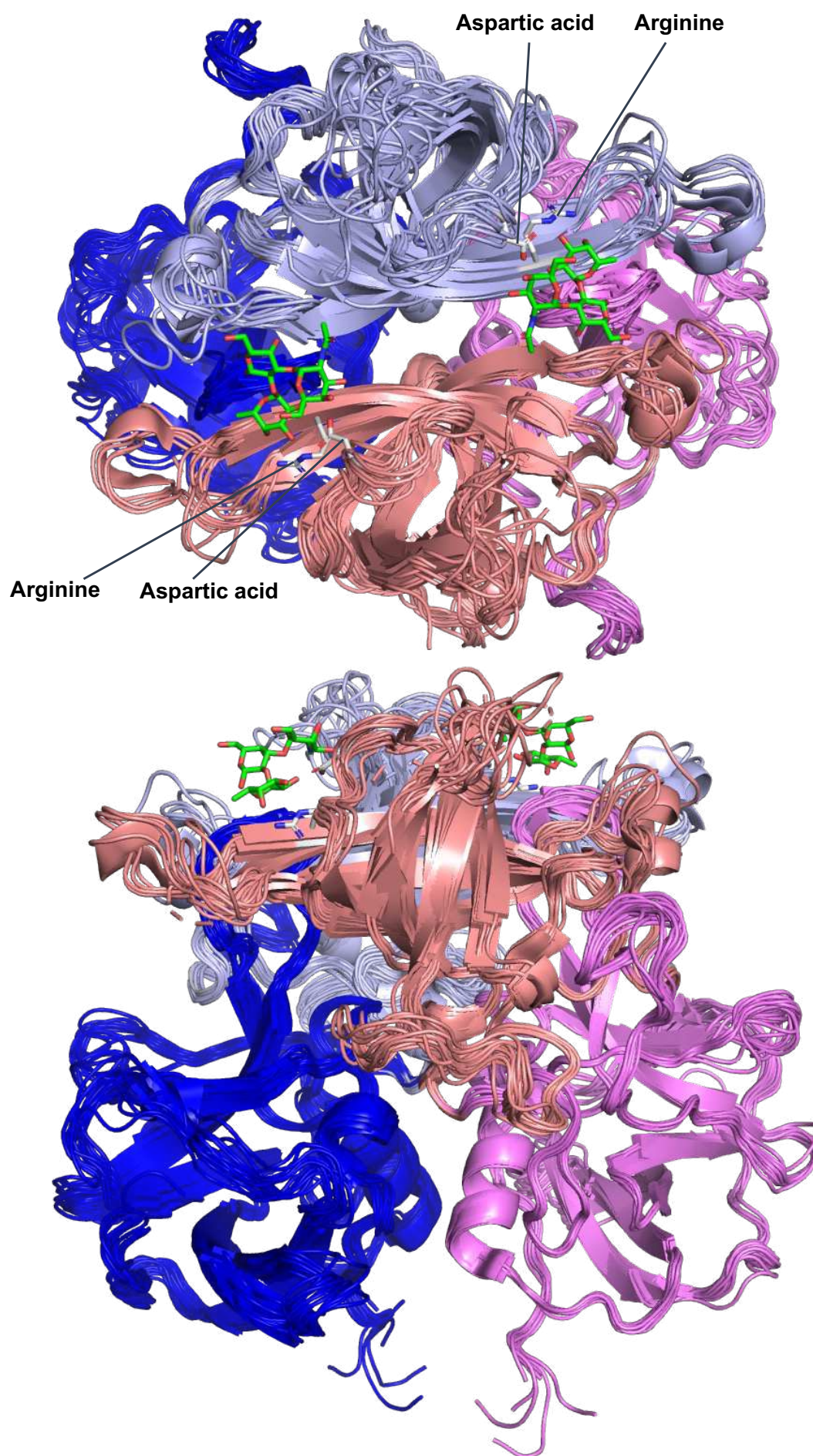
**2'-FL site 2 (powder)  
GII.10 P domain**



**2'-FL non-specific site (powder)  
GII.10 P domain**

**Figure S3. Representative simulated annealing difference omit maps.** The saccharides present in GII.4c P domain H2-type, GII.4-Syd P domain 2'-FL (powder) complex, GII.10 P domain 2'-FL (powder), GII.10 P domain 2'-FL (tablet) complex structures are shown and labeled fucose (Fuc), galactose (Gal), or glucose (Glc). The omit map (orange) is contoured between 2.5-2.0  $\sigma$ . The H2-type is a trisaccharide composed of an  $\alpha$ -L-fucose-(1-2)- $\beta$ -D-galactose-(3-1)-2-N-acetyl- $\alpha$ -D-galactosamine (only underlined portion was fitted into structure). The 2'-FL is a trisaccharide composed of an  $\alpha$ -L-fucose-(1-2)- $\beta$ -D-galactose-(1-4)- $\alpha$ -D-glucose.

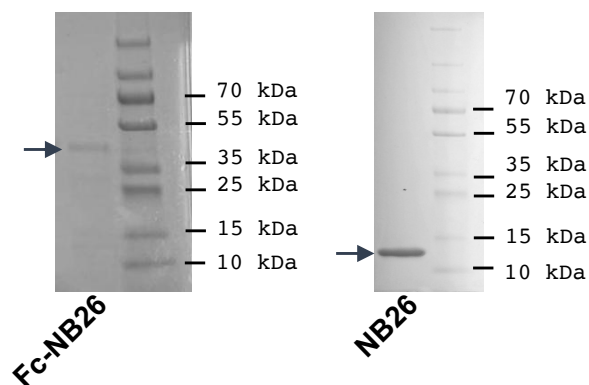
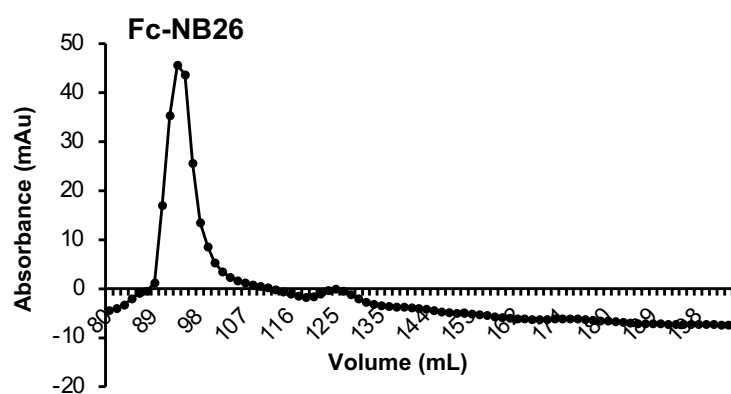
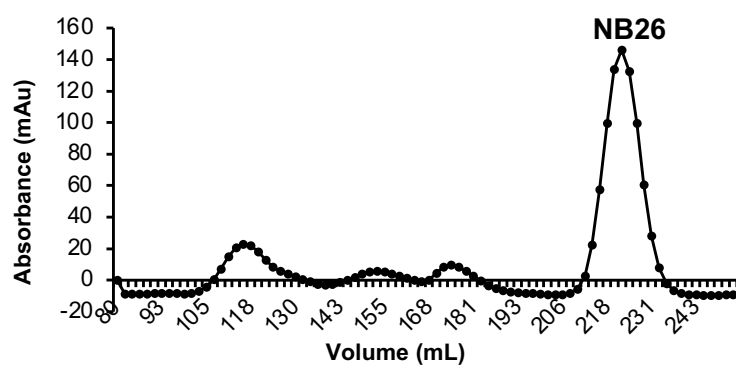




**Figure S4. Summary of GII P domains.** Fifteen P domains superimposed with the H2-type (green sticks) from the GII.4 Saga P domain H2-type complex structure (PDB ID: 4WZK) to show the HBGA pocket (Saga P domain removed). Structures are shown from top (top panel) and side (bottom panel) views. Two highly conserved side chain residues in all GII genotypes that interact with the fucose moieties found in HBGAs and HMO are shown as sticks and labeled.

**A**

QVQLQESGGGLVQPGGSLRLSCTAPRIIFFMYDVGWYRQAPEKQRELVAQINSDVS  
 TKYADSVKGRFTISRDNARNTVYLQMNDLKPEDAAVYYCNVRRASADYWGQGTQVT  
 VSSDKTHTCPPCPAPPELLGGPSVFLFPPKPKDTLMISRTPEVTCVVVDVSHEDPEV  
 KFNWYVDGVEVHNAKTKPREEQYNSTYRVVSVLTVLHQDWLNGKEYKCKVSNKALP  
 APIEKTISKAKGQPREPQVYTLPPSRDELTKNQVSLTCLVKGFYPSDIAVEWESNG  
 QPENNYKTTTPVLDSDGSFFLYSKLTVDKSRWQQGNVFCFSVMHEALHNHYTQKSL  
 SLSPGK

**B****C****D**

**Figure S5. Design and development of Fc-NB26.** (A) Amino acid sequence of NB26 (cyan) fused to a human IgG hinge (red) followed by human IgG Fc (green). (B) SDS-PAGE of Fc-NB26 (arrow showing Fc-NB26 monomer of 38.4 kDa) and NB26 (arrow showing NB26 of 15 kDa). (C) SEC graph of Fc-NB26 using a Superdex 75/200 column (D) SEC of NB26 using a Superdex 75/200 column.

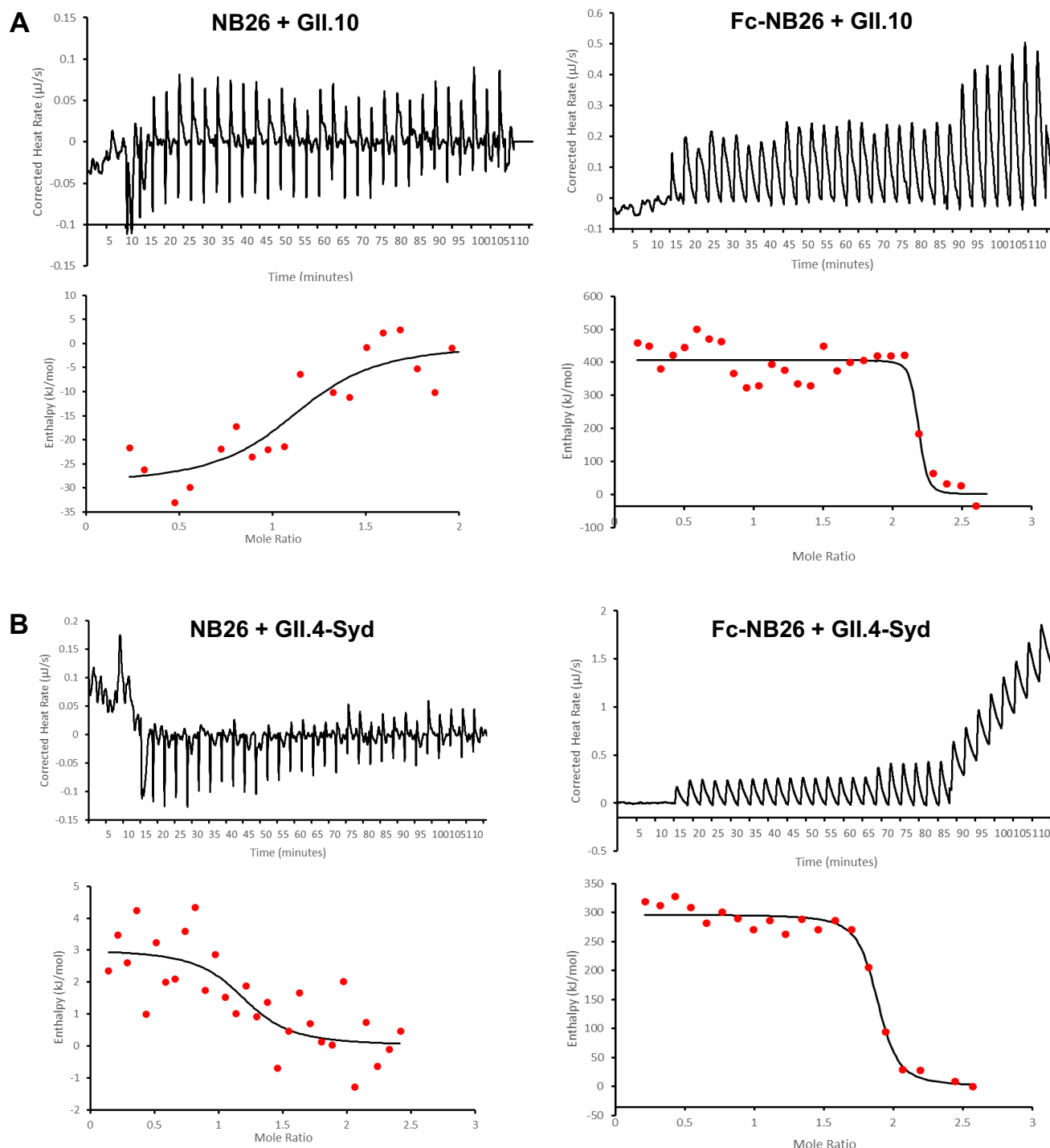


```

NB26 DVQLVESGGGLVQPGGSLRLSCTAPRIIFFMYDVGWYRQAPEKQRELVAQINSDVSTKYA 60
M4   QVKLQSGGGLVQPGGSLRLSCAASESTISINTLGWYRQAPGNQRELVAITTTGGTTNYA 60
      * *   ***** *   ***** *   * *
NB26 DSVKGRFTISRDNAKRTVYLMNDLKPEDAAVYYCNVRRAS-----ADYWGQGTQVTV 113
M4   DSVKGRFTISRDNAKNTVYLMNNLEPGDTAVYYCNLKRRDLQSRFGGYWGQGTQVTV 118
      ***** * * * ***** *   *****

```

**Figure S6. Amino acid alignment of NB26 and M4.** Amino acid sequence alignment of NB26 and M4, showing residues R26 and R100, respectively. The CDRs for NB26 (CDR1, 26-33; CDR2, 52-55; and CDR3, 98-108) and M4 (CDR1, 26-33; CDR2, 52-55, and CDR3, 98-108) are labeled and underlined.



**C**

P domain		NB26			Fc-NB26		
GII.10	K <sub>d</sub> (M)	4.41E-07	±	5.72E-08	8.24E-10	±	1.72E-10
	n	1.055	±	0.113	2.106	±	0.046
	ΔH (kJ/mol)	-28.41	±	1.29	340.80	±	94.33
	ΔS (J/mol.k)	26.43	±	5.40	1317.00	±	318.20
	K <sub>a</sub> (M <sup>-1</sup> )	2.28E+06	±	2.96E+05	1.24E+09	±	2.59E+08
GII.4-Syd	K <sub>d</sub> (M)	4.27E-07	±	1.09E-07	5.87E-09	±	3.77E-10
	n	1.062	±	0.052	1.818	±	0.016
	ΔH (kJ/mol)	19.66	±	1.92	282.20	±	20.22
	ΔS (J/mol.k)	188.00	±	8.63	1104.00	±	67.88
	K <sub>a</sub> (M <sup>-1</sup> )	2.37E+06	±	6.82E+05	1.71E+08	±	1.10E+07

**Figure S7. Thermodynamic properties of NB26 and Fc-NB26 binding to P domains using ITC.** NB26 or Fc-NB26 was titrated into (A) GII.10 P domain or (B) GII.4-Syd P domain. Examples of the titration (upper) of NB26 or Fc-NB26 to P domains are shown. The binding isotherm was calculated using a single binding site model (lower). (C) Constants K (binding constant in M<sup>-1</sup>), dH (heat change in cal/mol), dS (entropy change in cal/mol/deg), and dG (change in free energy in cal/mol) are shown with standard deviations. Fc-NB26 has significantly higher affinity (>100 fold higher) to these P domains than NB26 (Student's T-test, P value < 0.05).

**Table S1.** Data collection and refinement statistics for six GII genotype crystal structures

	GII.8 Amsterdam	GII.14 M7	GII.17 CS-E1
<b>Data collection</b>			
Space group	P2 <sub>1</sub> 2 <sub>1</sub> 2 <sub>1</sub>	C121	P12 <sub>1</sub> 1
Cell dimensions			
<i>a</i> , <i>b</i> , <i>c</i> (Å)	67.23, 78.43, 115.39	105.82, 91.83, 67.11	62.33, 72.03, 81.87
$\alpha$ , $\beta$ , $\gamma$ (°)	90.00, 90.00, 90.00	90.00, 92.98, 90.00	90.00, 111.02, 90.00
Resolution (Å)	46.68-1.73 (1.76-1.73)	49.02-1.44 (1.46-1.44)	45.26-1.27 (1.29-1.27)
<i>R</i> <sub>merge</sub> <sup>a</sup>	0.081 (0.588)	0.097 (1.675)	0.047 (0.284)
<I/σ(I)>	8.8 (1.4)	6.5 (0.6)	12.8 (3.0)
CC <sub>1/2</sub>	0.998 (0.810)	0.993 (0.163)	0.999 (0.927)
Completeness	99.2 (86.2)	98.4 (91.7)	99.7 (94.4)
Redundancy	5.9 (5.3)	3.4 (3.3)	5.3 (5.0)
<b>Refinement</b>			
Resolution (Å)	46.68-1.73 (1.79-1.73)	37.88-1.44 (1.49-1.44)	38.21-1.27 (1.32-1.27)
No. unique reflections	63983 (5990)	113706 (11362)	177023 (17213)
<i>R</i> <sub>work</sub> <sup>b</sup> / <i>R</i> <sub>free</sub> <sup>c</sup>	17.4/20.3 (26.4/32.3)	20.7/23.1 (32.6/34.7)	16.2/17.2 (18.8/19.7)
No. atoms	5445	5310	5682
Protein	4718	4711	4787
Water	723	587	860
Ligand	10	30	87
B-factors (Å <sup>2</sup> )	25.07	23.23	15.12
Protein	23.98	22.43	13.30
Water	32.09	29.52	24.86
Ligand	46.84	28.43	25.51
RMS bond length (Å)	0.006	0.009	0.005
RMS bond angle (°)	0.88	1.06	0.83
<b>Ramachadran Plot Statistics<sup>d</sup></b>			
Residues	602	602	612
Most Favored region	97.16	97.49	96.88
Allowed Region	2.84	2.34	3.12
Disallowed Region	0.00	0.17	0.00
Clashscore	4.86	3.45	2.53
<b>PDB ID</b>	8V95	8V96	8V97

$R_{\text{merge}} = [\sum_h \sum_i |I_h - I_{hi}| / \sum_h \sum_i I_{hi}]$  where  $I_h$  is the mean of  $I_{hi}$  observations of reflection  $h$ . Numbers in parenthesis represent highest resolution shell. <sup>b</sup>  $R_{\text{factor}} = \sum ||F_{\text{obs}}| - |F_{\text{calc}}|| / \sum |F_{\text{obs}}| \times 100$  for 95% of recorded data ( $R_{\text{factor}}$ ) or 5% data ( $R_{\text{free}}$ ). <sup>d</sup> Determined using MolProbity (10.1002/pro.3330)

**Table S1.** Data collection and refinement statistics for six GII genotype crystal structures

	GII.24 Loreto 1972	GII.26 Leon 4509	GII.NA1 Loreto 1257
<b>Data collection</b>			
Space group	P12 <sub>1</sub> 1	C121	P12 <sub>1</sub> 1
Cell dimensions			
<i>a</i> , <i>b</i> , <i>c</i> (Å)	60.75 80.82 70.98	129.44 71.17 78.59	62.70, 71.16, 78.39
$\alpha$ , $\beta$ , $\gamma$ (°)	90.00 113.62 90.00	90.00 109.92 90.00	90.00 110.04 90.00
Resolution (Å)	45.84-1.74 (1.77-1.74)	43.69-1.47 (1.50-1.47)	45.38-1.67 (1.69-1.67)
$R_{\text{merge}}^a$	0.053 (0.173)	0.078 (0.685)	0.118 (1.148)
$\langle I/\sigma(I) \rangle$	12.1 (4.3)	6.1 (0.9)	6.3 (0.8)
CC <sub>1/2</sub>	0.992 (0.949)	0.995 (0.476)	0.995 (0.453)
Completeness	98.8 (96.3)	98.8 (93.9)	99.5 (92.5)
Redundancy	3.0 (3.0)	2.9 (2.8)	4.6 (4.4)
<b>Refinement</b>			
Resolution (Å)	45.13-1.74 (1.80-1.74)	40.66-1.47 (1.53-1.47)	45.38-1.67 (1.73-1.67)
No. unique reflections	63597 (6227)	111572 (10859)	75029 (7469)
$R_{\text{work}}^b/R_{\text{free}}^c$	16.0/19.0 (19.5/24.2)	14.8/18.7 (27.4/30.9)	18.5/21.3 (29.7/32.7)
No. atoms	5699	5497	5338
Protein	4896	4796	4806
Water	763	515	456
Ligand	95	458	190
B-factors (Å <sup>2</sup> )	16.79	18.66	21.75
Protein	15.27	16.53	21.02
Water	25.61	29.38	27.45
Ligand	34.68	43.77	33.99
RMS bond length (Å)	0.008	0.014	0.011
RMS bond angle (°)	0.96	1.29	1.04
<b>Ramachadran Plot Statistics<sup>d</sup></b>			
Residues	617	616	618
Most Favored region	96.90	98.03	97.72
Allowed Region	3.10	1.97	2.28
Disallowed Region	0.00	0.00	0.00
Clashscore	5.67	3.44	2.28
<b>PDB ID</b>	8V98	8V99	8V9A

$R_{\text{merge}} = [\sum_h \sum_i |I_h - I_{hi}| / \sum_h \sum_i I_{hi}]$  where  $I_h$  is the mean of  $I_{hi}$  observations of reflection  $h$ . Numbers in parenthesis represent highest resolution shell. <sup>b</sup>  $R_{\text{factor}} = \sum ||F_{\text{obs}}| - |F_{\text{calc}}|| / \sum |F_{\text{obs}}| \times 100$  for 95% of recorded data ( $R_{\text{factor}}$ ) or 5% data ( $R_{\text{free}}$ ). <sup>d</sup> Determined using MolProbity (10.1002/pro.3330)

**Table S2.** Amino acid analysis of GII P domain X-ray crystal structures, where the P domain is further subdivided into P1-1, P2, and P1-2 subdomains.

Genotype name	Year	Species	P1	P2	Loop A (P2)	Loop B (P2)	Loop C (P1)	Loop D (P2)	GenBank	PDB
<b>GI.1 Hawaii</b>	1971	Human	223-277 401-539	278-400	339-344	371-380	434-441	393-394	U07611	4ROX
<b>GI.2 SMV</b>	1976	Human	223-277 408-539	278-407	339-351	377-387	441-448	400-401	AY134748	4RPB
<b>GI.3 TV24</b>	1991	Human	224-277 414-538	278-413	351-356	384-391	447-454	403-407	U02030	6IR5
<b>GI.4 Sydney-2012</b>	2012	Human	224-277 406-530	278-405	337-343	371-379	439-446	390-397	JX459908	4OOS
<b>GI.6 GuangXi</b>	2016	Human	224-267 403-526	268-401	339-359	376-383	436-443	405-406	OL468714	7YQG
<b>GI.8 Amsterdam</b>	1998	Human	227-278 403-527	279-402	340-345	373-380	436-443	391-396	AF195848	8V95
<b>GI.10 Vietnam026</b>	2000	Human	222-277 414-538	278-413	341-354	382-390	447-454	401-407	AF504671	3ONU
<b>GI.11 Sw918</b>	1997	Porcine	225-277 413-537	278-412	350-355	383-390	446-453	401-407	AB074893	6J0Q
<b>GI.12 Hiroshima</b>	1999	Human	222-277 401-525	278-400	339-344	372-380	434-441	390-393	AB044366	3R6J
<b>GI.14 M7</b>	1999	Human	226-278 402-524	279-401	338-344	372-379	435-442	390-396	AY130761	8V96
<b>GI.17 CS-E1</b>	2002	Human	224-278 406-530	279-402	340-348	376-383	439-446	393-400	AY502009	8V97
<b>GI.19 OH-QW170</b>	2003	Porcine	225-277 407-531	278-406	340-351	379-386	440-447	397-401	AAX32883	6GW4
<b>GI.24 Loreto1972</b>	2013	Human	225-279 408-533	280-407	341-353	382-388	442-449	398-403	KY225989	8V98
<b>GI.26 Leon4509</b>	2005	Human	224-277 408-532	278-407	340-352	380-387	441-448	396-402	KU306738	8V99
<b>GI.NA1 Loreto1257</b>	2013	Human	225-278 409-533	279-408	341-353	381-388	442-449	398-402	MG495079	8V9A

**Table S3.** Data collection and refinement statistics for GII.4c crystal structures

	GII.4c apo	GII.4c H2 type
<b>Data collection</b>		
Space group	P2 <sub>1</sub> 2 <sub>1</sub> 2 <sub>1</sub>	P2 <sub>1</sub> 2 <sub>1</sub> 2 <sub>1</sub>
Cell dimensions		
<i>a</i> , <i>b</i> , <i>c</i> (Å)	75.47, 90.56, 91.33	76.67 , 90.47, 91.34
$\alpha$ , $\beta$ , $\gamma$ (°)	90.00, 90.00, 90	90.00, 90.00, 90.00
Resolution (Å)	48.95-1.34 (1.37-1.34)	49.26-1.61 (1.64-1.61)
<i>R</i> <sub>merge</sub> <sup>a</sup>	0.072 (1.300)	0.071 (0.726)
<  <i>I</i> / $\sigma$ ( <i>I</i> )>	10.1 (0.9)	11.7 (1.7)
CC <sub>1/2</sub>	0.999 (0.609)	0.993 (0.769)
Completeness	99.7 (94.5)	99.9 (98.5)
Redundancy	8.9 (8.6)	6.8 (6.6)
<b>Refinement</b>		
Resolution (Å)	45.67-1.34 (1.39-1.34)	45.67-1.61 (1.67-1.61)
No. unique reflections	139399 (13446)	82629 (8124)
<i>R</i> <sub>work</sub> <sup>b</sup> / <i>R</i> <sub>free</sub> <sup>c</sup>	13.9/16.1 (23.4/26.0)	15.7/18.5 (21.5/26.5)
No. atoms	5333	5453
Protein	4720	4729
Water	512	669
Ligand	225	98
B-factors (Å <sup>2</sup> )	24.10	19.59
Protein	22.54	18.47
Water	34.55	26.78
Ligand	44.28	28.59
RMS bond length (Å)	0.008	0.008
RMS bond angle (°)	0.98	0.98
<b>Ramachadran Plot Statistics<sup>d</sup></b>		
Residues	612	612
Most Favored region	98.36	98.36
Allowed Region	1.64	1.64
Disallowed Region	0.00	0.00
Clashscore	2.23	1.82
<b>PDB ID</b>	8VRU	8VRV

$R_{\text{merge}} = [\sum_h \sum_i |I_h - \bar{I}_{hi}| / \sum_h \sum_i I_{hi}]$  where  $\bar{I}_h$  is the mean of  $I_{hi}$  observations of reflection  $h$ . Numbers in parenthesis represent highest resolution shell. <sup>b</sup>  $R_{\text{factor}} = \sum ||F_{\text{obs}}| - |F_{\text{calc}}|| / \sum |F_{\text{obs}}|$  x 100 for 95% of recorded data ( $R_{\text{factor}}$ ) or 5% data ( $R_{\text{free}}$ ). <sup>d</sup> Determined using MolProbity (10.1002/pro.3330)

**Table S4.** Data collection and refinement statistics for GII.4-Syd 2'-FL and GII.10 2'-FL complex crystal structures

	<b>GII.4-Syd 2'-FL (powder)</b>	<b>GII.10 2'-FL (powder)</b>	<b>GII.10 2'-FL (tablet)</b>
<b>Data collection</b>			
Space group	C121	P12 <sub>1</sub> 1	P12 <sub>1</sub> 1
Cell dimensions			
<i>a</i> , <i>b</i> , <i>c</i> (Å)	98.62, 55.76, 63.61	67.99, 78.70, 70.77	65.41, 78.93, 70.07
$\alpha$ , $\beta$ , $\gamma$ (°)	90.00, 120.14, 90.00	90.00, 102.83, 90.00	90.00, 101.13, 90.00
Resolution (Å)	47.02-1.54 (1.56-1.54)	44.63-1.47 (1.49-1.47)	43.55-1.41 (1.43-1.41)
$R_{\text{merge}}^a$	0.060 (0.841)	0.059 (1.150)	0.054 (1.097)
$\langle I/\sigma(I) \rangle$	11.1 (1.1)	9.2 (0.7)	9.0 (0.7)
$CC_{1/2}$	0.999 (0.601)	0.999 (0.395)	0.998 (0.506)
Completeness	95.3 (86.6)	99.0 (84.1)	99.4 (93.7)
Redundancy	4.8 (4.6)	4.5 (4.3)	4.5 (4.2)
<b>Refinement</b>			
Resolution (Å)	41.69-1.54 (1.60-1.54)	39.35-1.47 (1.52-1.47)	43.55-1.41 (1.46-1.41)
No. unique reflections	42167 (4114)	122514 (11652)	133809 (13194)
$R_{\text{work}}^b/R_{\text{free}}^c$	15.5/18.3 (25.6/30.4)	16.7/19.1 (28.8/30.5)	17.1/19.5 (34.7/35.4)
No. atoms	2766	5681	5444
Protein	2373	4792	4763
Water	340	688	597
Ligand	59	353	154
B-factors (Å <sup>2</sup> )	19.73	24.43	25.88
Protein	18.42	23.06	24.80
Water	27.97	32.85	33.20
Ligand	25.28	28.26	35.18
RMS bond length (Å)	0.009	0.009	0.009
RMS bond angle (°)	1.06	1.00	1.01
<b>Ramachadran Plot Statistics<sup>d</sup></b>			
Residues	308	625	623
Most Favored region	97.71	97.25	97.24
Allowed Region	2.29	2.75	2.76
Disallowed Region	0.00	0.00	0.00
Clashscore	1.90	4.97	1.99
<b>PDB ID</b>	<b>8Y5V</b>	<b>8Y6C</b>	<b>8Y6D</b>

$R_{\text{merge}} = [\sum_h \sum_i |I_h - I_{hi}| / \sum_h \sum_i I_{hi}]$  where  $I_h$  is the mean of  $I_{hi}$  observations of reflection  $h$ . Numbers in parenthesis represent highest resolution shell. <sup>b</sup>  $R_{\text{factor}} = \sum ||F_{\text{obs}}| - |F_{\text{calc}}|| / \sum |F_{\text{obs}}|$  x 100 for 95% of recorded data ( $R_{\text{factor}}$ ) or 5% data ( $R_{\text{free}}$ ). <sup>d</sup> Determined using MolProbity (10.1002/pro.3330)